nature nanotechnology

Article

https://doi.org/10.1038/s41565-026-02208-y

Halide-site-substituting spacer creates quasi-two-dimensional perovskites for vapour-deposited light-emitting diodes

Received: 6 September 2025

Accepted: 20 May 2026

Published online: 01 July 2026

Check for updates

Chan-Yul Park[1,7], Joo Sung Kim[1,2,3,7], Xian Wei Chua[2,3,7], Eojin Yoon[1], Young-Kwang Jung[2,3], Jaehyun Song[1], Min-Jun Sung[1], Hyun-Wook Kim[1], Woo Jin Jeong[1], Seong Eui Chang[1], Jinwoo Park[1], Bo-Hyun Choi[1], Somin Kim[1], Kyoo-Hyung Lee[1], Samuel D. Stranks[2,3] ✉ & Tae-Woo Lee[1,4,5,6] ✉

Vapour deposition offers a scalable and industry-compatible route for perovskite light-emitting diodes, yet the process remains challenging owing to kinetically driven crystallization that produces mixed-dimensional phases and nanoscale heterogeneity. In particular, the lack of thermodynamic control leads to phase-disordered nanostructures, broadened energy landscapes and limited device efficiency. Here we report a thermodynamically guided vapour-phase synthesis of X-type quasi-two-dimensional perovskites, $(CsPbBr_3)_{n-1}Cs_2PbBr_2X_2$, with controlled nanoscale phase distribution and interfacial coherence. By introducing a halide-site-substituting organic spacer molecule that covalently binds to Pb^{2+} during in situ deposition, we achieve selective crystallization of quasi-two-dimensional phases with high phase purity. A self-assembled hetero-scaffold of LiF and spacer molecule acts as a nanoscale growth template, promoting spatially uniform nucleation and minimizing phase segregation. Multimodal structural and spectroscopic analyses reveal dimensionally and spatially homogeneous films with high photoluminescence quantum yield (>85%) and reduced trap densities, enabling efficient exciton confinement and narrow emission. The resulting perovskite light-emitting diodes achieve an external quantum efficiency of 21.9%, an electroluminescence linewidth of 78.5 meV and operational stability exceeding 1,500 min, with scalable pixel arrays demonstrated. These results provide a scalable route to high-efficiency vapour-deposited perovskite optoelectronics.

Metal halide perovskites are promising emitters for next-generation displays owing to their high colour purity, tunable emission, high photoluminescence quantum yield (PLQY) and low material cost[1–4]. Recent perovskite light-emitting diodes (PeLEDs) have achieved external quantum efficiency (EQE) exceeding 20%, particularly through solution processing[5–7]. However, as seen in organic light-emitting diodes (OLEDs) commercialization, industrial display manufacturing ultimately requires vapour deposition for high reproducibility and precise control over film thickness, composition and large-area uniformity. Therefore, developing vapour-deposited perovskite emitters is highly attractive, especially because this approach is compatible with existing OLED production infrastructure, whereas conventional quantum-dot emitters remain limited to solution-processing methods.

However, unlike the physical vapour deposition used for OLEDs, perovskite vapour deposition involves in situ chemical reactions among precursors arriving at the substrate, making it closer to a

A full list of affiliations appears at the end of the paper. ✉e-mail: sds65@cam.ac.uk; twlees@snu.ac.kr

chemical vapour deposition process; as a result, achieving high-quality perovskite films in the vapour phase remains fundamentally challenging owing to complicated reaction routes[8–10]. Furthermore, unlike solution processes that exploit solvent coordination to guide crystallization pathways, vapour-phase systems lack such solvent-mediated kinetic modulation strategies. Consequently, precursors with high kinetic energies undergo rapid surface reactions, leading to kinetically driven growth without energetic selectivity[11]. Multiple low-barrier interactions, including van der Waals forces, hydrogen bonding and weak coordination[12,13], can therefore compete simultaneously, producing broad distributions of 0D, low-n (n = 1–4), medium-n ($n \geq 5$), 3D ($n = \infty$) and intermediate phases, thereby inherently limiting phase selectivity[14,15].

This lack of dimensional or phase selectivity is particularly detrimental in LED applications, where confined nanostructures (for example, nanocrystals and quasi-two-dimensional (quasi-2D) perovskites) are essential for efficient radiative recombination. Broad phase distributions generate inhomogeneous energy landscapes, spectral broadening and non-radiative carrier recombination, limiting the EQEs of vapour-deposited PeLEDs still below those of solution-processed devices. Overcoming this limitation requires a change in vapour-synthesis design from kinetic modulation of precursor interactions to thermodynamically guided reaction pathways. Particularly in confined nanostructures of metal halide ABX_3 structure (A = organic or inorganic cation; B = divalent metal cation; X = halide anion), the nature of surface-interacting spacer ligands can critically influence crystallization pathways and phase distribution. However, conventional quasi-2D systems based on A-site-substituting organic spacers (A-type spacers), which rely on weak hydrogen bonding, provide limited control over vapour-phase crystallization. This limitation motivates the use of X-site-substituting organic spacers (X-type spacers), where stronger covalent bonding with the central metal provides a phase-selective route for quasi-2D perovskite growth.

In this work, we report vapour-phase-synthesized X-type quasi-2D perovskites ($(CsPbBr_3)_{n-1}Cs_2PbBr_2X_2$), where X-type spacers act as covalently bonded organic spacers. Substrate back-heating promotes thermodynamically selective crystallization by forming strong covalent bonds, suppressing kinetically driven mixed phases and enabling a narrow phase distribution. The same X-type spacer forms a self-assembled scaffold covalently integrated with a lithium fluoride (LiF) layer, guiding quasi-2D perovskite crystallization with structural continuity while ensuring both dimensional and spatial homogeneity down to the microscale. The resulting films showed a high PLQY of 85% and narrow emission with a full-width at half-maximum (FWHM) of 17 nm. By leveraging homogeneously distributed X-type quasi-2D perovskites, PeLEDs demonstrated ultra-narrow electroluminescence (EL) spectra with a linewidth of 78.5 meV and an EQE of 21.9%, representing the highest efficiency reported for vapour-deposited PeLEDs. Large-area pixelated devices with 10 × 10 arrays demonstrate the scalability and industrial relevance of this vapour deposition strategy.

Vapour-phase synthesis of X-type quasi-2D perovskites

The vapour-phase synthesis of quasi-2D perovskites was accomplished by co-deposition of CsBr, $PbBr_2$ and either phenethylammonium bromide (PEABr) (for A-type quasi-2D perovskites, $(CsPbBr_3)_{n-1}A_2PbBr_4$) or BPA (for X-type quasi-2D perovskites) for comparison purposes. To utilize the synergistic effect of the high kinetic energy of surface-adsorbed precursors and the thermal energy required to overcome the activation energy (E_a), we used in situ substrate back-heating during vapour deposition in vacuum (Fig. 1a). The conventional post-annealing provides thermal energy only after the precursors have lost their kinetic energy, leaving non-perovskite intermediate phases such as unreacted precursors or polybromide complexes[16,17] (Supplementary Fig. 1). This highlights the need for concurrent kinetic and thermal energy for effective quasi-2D crystallization.

First, density functional theory (DFT) calculations revealed that X-type quasi-2D perovskite $Cs_2PbBr_2(BPA)_2$ has an n = 1 layer spacing of 18.3 Å, larger than the 16.3 Å spacing of conventional A-type quasi-2D perovskite PEA_2PbBr_4. This expanded lattice arises because BPA directly coordinates to Pb^{2+} by occupying halide-equivalent sites, thereby forming a layered nanostructure (Fig. 1a).

The X-type quasi-2D perovskite structure was confirmed by grazing-incidence wide-angle X-ray scattering (GIWAXS) analysis, exhibiting a pronounced diffraction peak at $q = 0.35$ Å^{-1} that corresponds to an out-of-plane d-spacing of 18.0 Å (Extended Data Fig. 1), closely matching the DFT-predicted results. These structural features were supported by morphological analysis of ultra-thin films, distinguishing the X-type quasi-2D phases from previously reported A-type quasi-2D phases[5] (Supplementary Figs. 2 and 3).

The binding mode of BPA within the X-type quasi-2D perovskite lattice was investigated with X-ray photoelectron spectroscopy (XPS). XPS O 1*s* spectra revealed the formation of a covalently bonded P–O–Pb species, indicating coordination of deprotonated BPA to Pb^{2+} at halide-equivalent sites[5,18,19] (Extended Data Fig. 2a–f and Supplementary Fig. 4). Fourier transform infrared (FTIR) spectroscopy and solid-state ^{31}P nuclear magnetic resonance (NMR) also support this, showing a P–O–Pb vibration and chemisorbed monodentate BPA^- species, respectively[20–22] (Extended Data Fig. 2g,h). These results provide spectroscopic evidence for the formation of an X-type quasi-2D structure, where the anionic phosphonate organic spacer occupies a halide-equivalent site through covalent bonding.

The temperature-dependent crystallization of the A-type and X-type quasi-2D systems was examined under varied back-heating temperatures by quantifying the relative phase contributions from their ultraviolet–visible (UV–Vis) absorption spectra[23,24] (Extended Data Fig. 3 and Supplementary Fig. 5). Within the back-heating temperature of 298–333 K, A-type quasi-2D films exhibited mixed phase distributions with substantial portions of unreacted intermediate phases, medium-n phases and even a small amount of low-n phases (Fig. 1b). Upon heating to 343 K, the intermediates were converted mainly into 0D Cs_4PbBr_6 phases (proportion of >50%), indicating that A-type quasi-2D phases form easily at low temperature owing to low formation barriers but are also highly susceptible to thermally induced disproportionation (Fig. 1b).

By contrast, BPA-based X-type quasi-2D films retained substantial amounts of intermediate phases up to 343 K, indicating that strong $PbBr_2$–BPA interactions thermodynamically stabilize the intermediate state and retard crystallization (Fig. 1c). Only at a higher back-heating temperature of ~353 K, the intermediate phases fully converted into medium-n phases. Low-n phases appeared only above 373 K, while 0D phases were not observed even at 393 K, indicating that strong P–O–Pb bonding increases the E_a and enables thermodynamic phase pinning of high-purity quasi-2D phases. Those medium-n phases also showed improved phase stability and emission tunability, benefiting from narrow phase distribution without undesired unstable phases (Supplementary Figs. 6 and 7).

Schematic phase diagrams summarize the temperature-dependent crystallization pathways of A-type and X-type quasi-2D systems (upper panel of Fig. 1d,e). While A-type systems undergo intermediate phase mixing or thermal de-trapping, X-type systems exhibit thermodynamic phase pinning at 343–373 K, where medium-n phases are selectively stabilized and resist de-trapping into low-n phases even at elevated temperatures.

These trends are also reflected in the optical properties (bottom panel of Fig. 1d–e). A-type quasi-2D films showed a PLQY of ~40% at low temperature but broad emission (FWHM of ~100 meV) owing to mixed phases, followed by decreased PLQY at higher temperatures as bulky 3D and non-emissive 0D phases formed. However, BPA-based films

https://doi.org/10.1038/s41565-026-02208-y

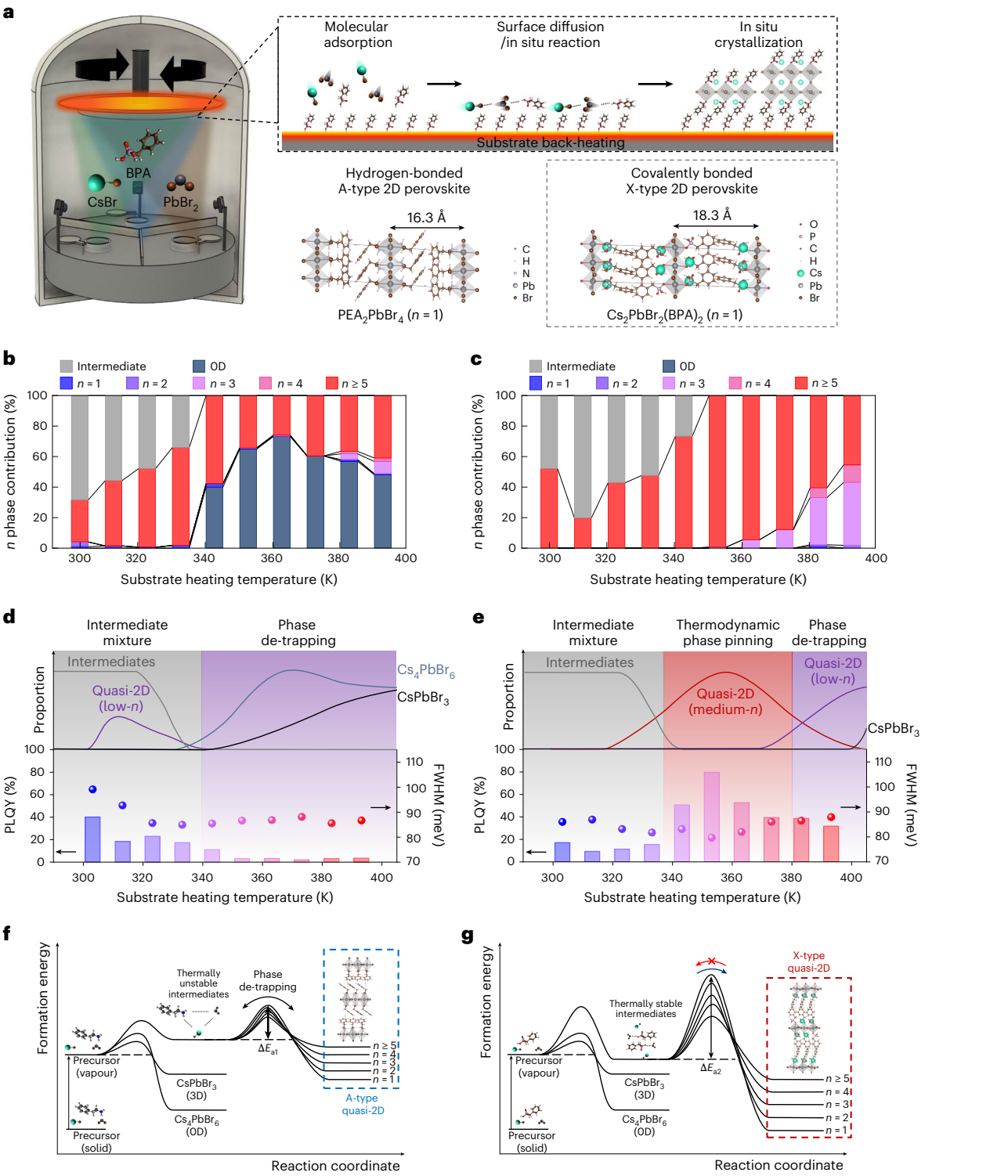

Fig. 1 | Vapour-phase synthesis of A-type and X-type quasi-2D perovskites. **a**, Schematic illustration of the vapour-deposition process for perovskite films, alongside structural model of A-type and X-type quasi-2D perovskite structure. **b**,**c**, *n*-phase contribution of vapour-phase synthesized A-type (**b**) and X-type (**c**) quasi-2D perovskites using the second-derivative UV–Vis absorption spectra at different back-heating temperatures. **d**,**e**, Schematic phase proportion (upper panel) and corresponding PLQY and FWHM (bottom panel) of A-type (**d**) and X-type (**e**) quasi-2D perovskite films at different back-heating temperatures. **f**,**g**, Schematic phase diagrams on reaction kinetics of vapour-phase synthesis for A-type (**f**) and X-type quasi-2D perovskites (**g**).

achieved high PLQY (~80%) and narrow emission (FWHM of <80 meV) at 343–373 K, where selective medium-*n* phases enabled both exciton confinement and a narrow energy distribution. Moreover, X-type quasi-2D perovskite films showed a 10-fold longer photostability than A-type quasi-2D films (Extended Data Fig. 4).

These crystallization pathways can be visualized as a chemical reaction coordinate diagrams (Fig. 1f,g). In the A-type quasi-2D system, a low activation barrier (low E_{a1} ~ RT) leads to formation of a quasi-2D structure near room temperature but also promotes reverse disproportionation into 0D or intermediate phases, resulting

in a kinetically trapped multiphase mixture. By contrast, the X-type quasi-2D system forms a thermally stable intermediate with a higher activation barrier (high E_{a2}), enabling thermodynamically selected phases that resist phase de-trapping. These results highlight thermodynamically guided phase selection as a promising strategy to overcome the inherent limitations of kinetically governed vapour-phase crystallization.

Self-assembled hetero-scaffold for X-type quasi-2D perovskites with homogeneous light emission

Another critical challenge in vapour-deposited perovskites is inhomogeneous crystallization at the substrate interface[25]. Differences in sticking and diffusion coefficients between organic and inorganic precursors[26–28], together with the self-assembly of 2D spacer molecules[29–31], can cause non-uniform morphology and broad phase distributions. In practice, X-type quasi-2D perovskite films also exhibited poor morphology with highly segregated phases on most conventional organic charge transport layers for fabrication of PeLEDs (Supplementary Figs. 8 and 9). To address this issue, we introduced a vapour-deposited LiF/BPA scaffold (hetero-scaffold) to promote uniform perovskite crystallization during film growth.

The XPS analysis of each LiF, BPA and hetero-scaffold showed that the hetero-scaffold exhibited a distinct additional peak at 531.0 eV, indicating the formation of self-assembled BPA on the LiF layer through covalent P–O–Li bonds[32,33] (Supplementary Fig. 10a,b). Contact angle measurements showed that the surface energy of the hetero-scaffold was lower than that of the BPA scaffold, supporting the preferential upward orientation of the benzene rings owing to improved uniformity induced by the underlying LiF layer[34–36] (Supplementary Fig. 11 and Supplementary Table 1). Kelvin probe force microscopy (KPFM) and atomic force microscopy (AFM) analyses also confirmed that the surface of the hetero-scaffold possessed a uniform surface potential and low surface roughness (Extended Data Fig. 5 and Supplementary Table 2), suggesting that the hetero-scaffold improves both the chemical and morphological uniformity of the substrate interface.

The effect of different scaffold structures on the optical properties and phase distribution of the vapour-deposited perovskite films was further investigated (Extended Data Fig. 6 and Supplementary Fig. 12). The overall temperature-dependent trend of phase distribution of the evaporated perovskites to achieve the best film in terms of PLQY and FWHM at 353 K remains similar irrespective of the use of scaffolds; however, the films without a scaffold (PLQY = 39%, FWHM = 81.2 meV) and with the BPA scaffold (PLQY = 55%, FWHM = 80.9 meV) exhibited lower PLQY, broader emission linewidths and increased formation of undesired phases compared with the perovskite film on the hetero-scaffold. These results suggest that the uniform surface of hetero-scaffold promotes more selective and homogeneous crystallization into unified quasi-2D phases, minimizing residual phases and thereby enhancing exciton confinement and narrowing the energy distribution.

To examine the influence of microscale interfacial heterogeneity on the optoelectronic properties, we performed wide-field hyperspectral microscopy on quasi-2D perovskite films with different scaffolds (Fig. 2a–c). Specifically, we compared PL intensities at 460 nm ($n = 3$, upper panel) and 515 nm ($n \geq 5$, middle panel) and calculated their PL intensity ratio (PL_{460}/PL_{515}, bottom panel) to visualize micrometre-scale spatial distribution of low-n phases. In quasi-2D perovskite films without a scaffold, inhomogeneous large grains were observed with strong emission centred at 460 nm; additional emission peaks corresponding to $n = 2$, 3 and 4 were also observed in spatially localized regions, indicating pronounced phase segregation of low-n phases (Fig. 2a,d). Quasi-2D perovskite films with the BPA scaffold also showed locally segregated low-n phases with inhomogeneous emission profiles, indicating partial improvement but still incomplete suppression of phase segregation (Fig. 2b,e).

By contrast, quasi-2D perovskite films with the hetero-scaffold exhibited narrow emission features of medium-n ($n \geq 5$) phases centred at 515 nm across the entire mapped area (Fig. 2c,f), demonstrating that the hetero-scaffold enables spatially homogeneous PL emission dominated by medium-n ($n \geq 5$) phases without any contribution from low-n phases even at the microscale (Fig. 2g). The centre-of-mass PL wavelength maps and corresponding histograms also revealed a much more uniform emission profile across the entire area of perovskite films with the hetero-scaffold, compared with that of perovskite films both without and with the BPA scaffold (Extended Data Fig. 7). This phase segregation in perovskite films without and with the BPA scaffold results from non-uniform crystallization caused by the random separation of BPA spacers in perovskites and local deviations from stoichiometry during film growth. Also, the confocal time-resolved PL lifetime imaging on the hetero-scaffold films (Supplementary Fig. 13) revealed highly uniform PL decay behaviour, indicating consistent carrier kinetics arising from spatial phase uniformity on the micrometre scale. The morphology of perovskite films observed from scanning electron microscope (SEM) and AFM analyses confirmed the highly uniform growth of quasi-2D perovskites on the hetero-scaffold (Supplementary Figs. 14 and 15). Especially, perovskite films grown on the hetero-scaffold exhibited a consistent Br:Pb ratio and phase across the entire film, while perovskite films without or with the BPA scaffold exhibited highly inhomogeneous regions with substantially deviated Br:Pb ratios from energy-dispersive X-ray spectroscopy (EDS) (Extended Data Fig. 8, Supplementary Figs. 16–18 and Supplementary Table 3). These results highlight that the hetero-scaffold effectively mitigates phase broadening during vapour-phase crystallization, enabling spatially homogeneous quasi-2D films essential for high-efficiency light emission[37].

Structural and optical properties of X-type quasi-2D perovskite films

To clarify how scaffold-induced phase differences affect structural and carrier recombination properties, we performed GIWAXS analysis with complementary PL characterization. The perovskite films grown without and with the BPA scaffold exhibited diffraction peaks corresponding to low-n, 0D and 3D phases (Fig. 3a,b and Supplementary Fig. 19). Moreover, perovskite films deposited on the LiF-only scaffold showed no GIWAXS signatures of low-n phases and exhibited PL emission at the band edge of the 3D phases, indicating that LiF alone is insufficient to induce quasi-2D phase formation (Supplementary Fig. 20). By contrast, in the perovskite film with the hetero-scaffold, the diffraction peak of medium-n phases became dominant without any low-dimensional phases (Fig. 3c), indicating a well-controlled phase distribution with suppressed formation of undesired phases. Here the hetero-scaffold provides the necessary interfacial conditions for controlled uniform growth of medium-n quasi-2D phases. Morphological analysis of the ultra-thin evaporated films of each individual precursor (CsBr, $PbBr_2$ and BPA) further revealed how different scaffolds influence the initial stages of adsorption, diffusion and crystallization, leading to distinct phase distributions (Supplementary Figs. 21–23). Uniform adsorption and distribution of all individual precursors could be achieved only on the hetero-scaffold, promoting homogeneous stoichiometric reactions and the formation of phase-uniform X-type quasi-2D perovskites, which could not be achieved without a scaffold or on other single scaffolds.

Transient absorption (TA) spectroscopy further supports the scaffold-dependent phase distribution in perovskite films (Fig. 3d–f and Supplementary Fig. 24). Unlike the 3D perovskite film (Supplementary Fig. 25), the quasi-2D perovskite film grown without a scaffold shows distinct bleach peaks at 455 nm ($n = 3$) and 475 nm ($n = 4$), indicating low-n phases (Fig. 3d). These bleach peaks became less visible in the quasi-2D perovskite film with the BPA scaffold (Fig. 3e), consistent with partial improvement but still incomplete suppression of phase segregation. By contrast, these peaks were

https://doi.org/10.1038/s41565-026-02208-y

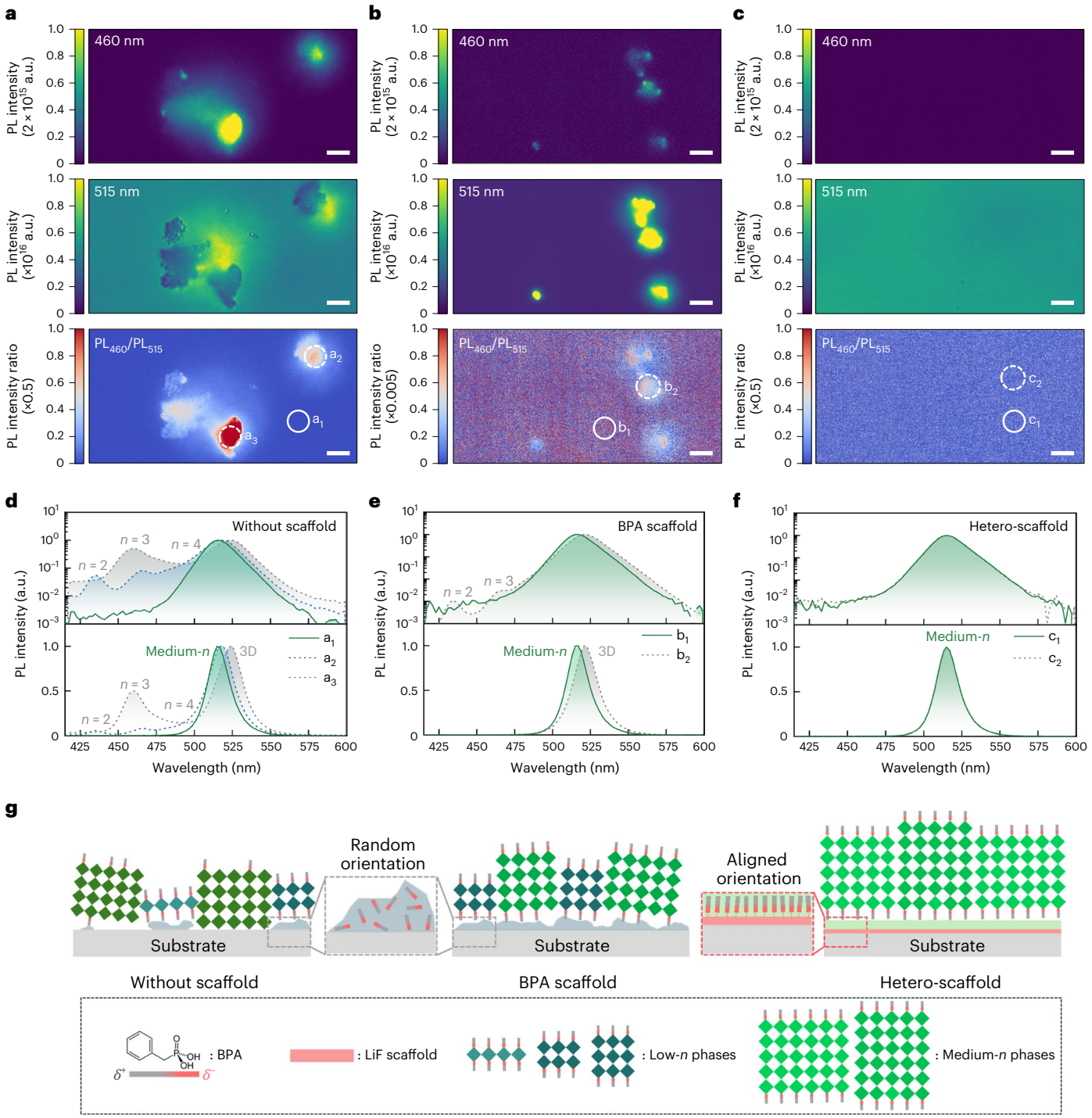

Fig. 2 | Effect of self-assembled scaffold on the emission homogeneity of X-type quasi-2D perovskite films. a–**c**, Hyperspectral PL mapping images under 405 nm excitation, showing the PL intensity at 460 nm (upper panel), 515 nm (middle panel) and the ratio of PL intensity between 460 nm and 515 nm (PL_{460}/PL_{515}) (bottom panel) for perovskite films without a scaffold (**a**), with the BPA scaffold (**b**) and with the LiF/BPA hetero-scaffold (**c**). Scale bars, 5 µm. **d**–**f**, PL emission spectra of perovskite films grown without a scaffold (**d**), on the BPA scaffold (**e**) and on the LiF/BPA hetero-scaffold (**f**), extracted from selected regions in **a**–**c**, respectively. **g**, Schematic illustration of the growth of quasi-2D perovskites without a scaffold (left), with the BPA scaffold (middle) and with the LiF/BPA hetero-scaffold (right).

almost non-discernible for the quasi-2D perovskite film with the hetero-scaffold, suggesting well-controlled phase distribution with suppressed formation of low-*n* phases (Fig. 3f). The insets in Fig. 3d,e show the kinetics of the 455 nm ($n = 3$) bleach feature with total rise times of ~426 fs and ~367 fs for the films without and with the BPA scaffold, respectively, followed by rapid decay within ~500 fs, indicating the carrier funnelling towards lower-energy phases.

Further, the magnified TA spectra around the main bleach features were used to examine the phase distribution from medium-*n* ($n \geq 5$) to bulk-like 3D regimes (Supplementary Fig. 26). Additional bleach side peaks were resolved and assigned to $n = 5$–9 phases, consistent with bandgap estimations from the effective-mass approximation (Supplementary Fig. 27). Whereas perovskite films without or with the BPA scaffold showed broad bleach features extending to

https://doi.org/10.1038/s41565-026-02208-y

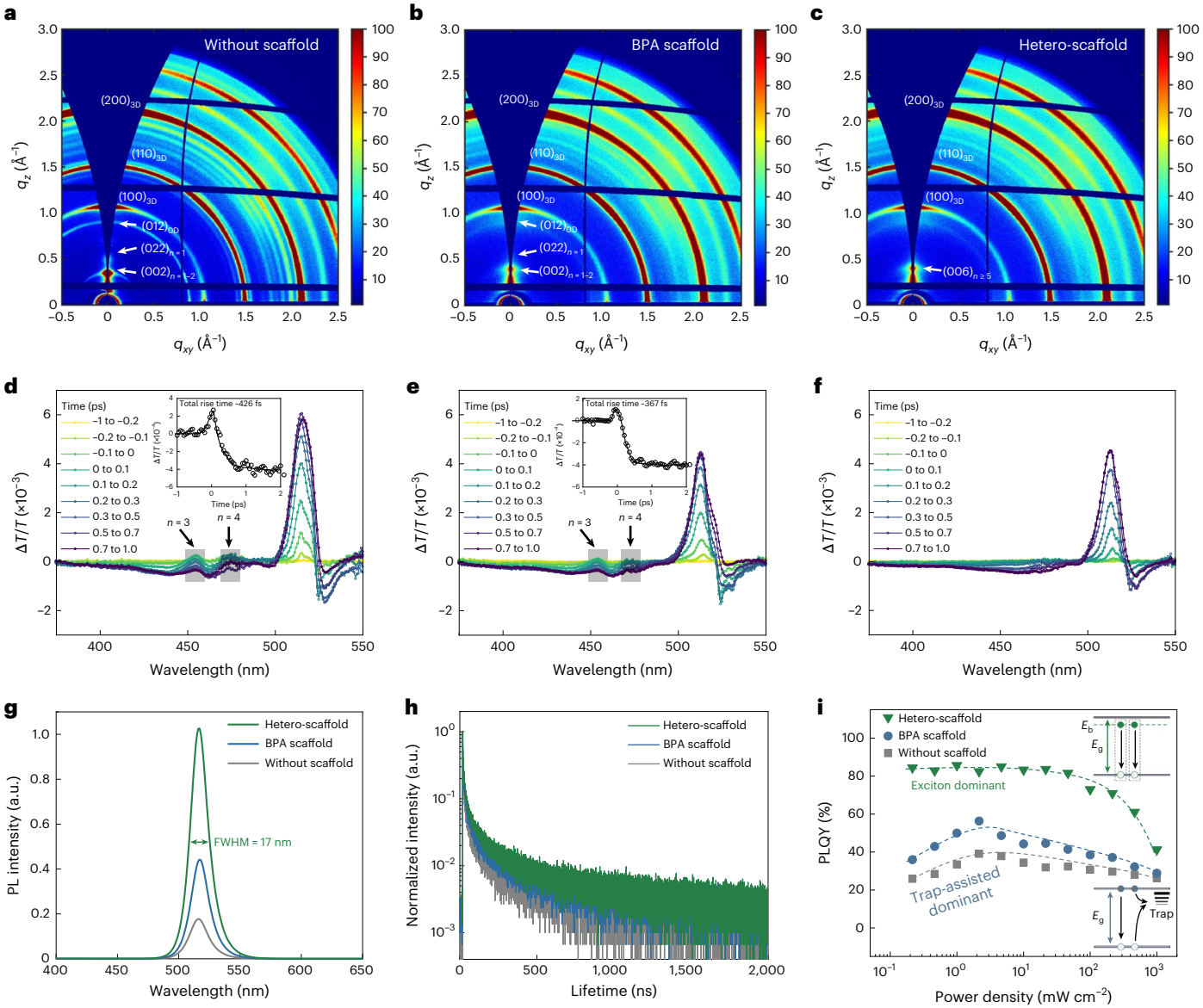

Fig. 3 | Structural and optical properties of X-type quasi-2D perovskite films. **a**–**c**, GIWAXS 2D patterns of perovskite films without a scaffold (**a**), with the BPA scaffold (**b**) and with the hetero-scaffold (**c**). **d**–**f**, Transient absorption spectra of quasi-2D perovskite films at selected pump–probe time delays (as labelled) within the first ps without a scaffold (**d**), with the BPA scaffold (**e**) and with hetero-scaffold (**f**). The films were excited at 355 nm (fluence 16.8 μJ cm^{-2}). Insets in **d** and **e** show the rise and decay kinetics of the 455 nm bleach feature ($n = 3$). **g**, PL emission spectra of perovskite films. **h**, Time-correlated single-photon counting spectra at 515 nm of perovskite films (λ_{exc} = 398 nm, fluence 0.624 nJ cm^{-2}). **i**, Fluence-dependent PLQY measurement of perovskite films (λ_{exc} = 405 nm).

522 nm ($n = 9$), the perovskite film on hetero-scaffold exhibited narrower bleach signals limited to ~517 nm ($n = 7$), indicating a narrower medium-n phase distribution ($n = 5$–7) without extension to higher-n or bulk-like 3D phases.

In terms of the radiative recombination process, perovskite films grown on the hetero-scaffold exhibited the highest PLQY, a longer PL lifetime and the longest transient absorption decay time at the main bleach region (510–520 nm), indicating reduced trap density and enhanced radiative recombination (Fig. 3g,h and Supplementary Fig. 28). Notably, the perovskite films grown without or with the BPA scaffold showed low PLQY at low carrier densities where trap-assisted recombination dominated over radiative recombination, likely owing to inefficient carrier confinement and trap states originating from segregated bulk-like 3D phases and defective surfaces (Fig. 2d,e). By contrast, perovskite films with hetero-scaffold maintained a high PLQY of >85% even at low carrier densities (Fig. 3i), indicating strong exciton confinement within the homogeneously distributed medium-n phases[38,39]. Also, the space-charge-limited current measurements revealed a lower trap density for the hetero-scaffold sample than for samples without or with the BPA scaffold, which can be attributed to effective surface passivation in medium-n phases without forming segregated bulk-like 3D phases or defective surfaces (Supplementary Fig. 29 and Supplementary Table 4).

Further, temperature-dependent PL analysis showed that the hetero-scaffold sample exhibited a much higher thermal activation energy (E_a) for PL quenching than the samples without a scaffold or with the BPA scaffold. This indicates that narrow-distributed medium-n phases suppress non-radiative recombination, exciton dissociation associated with charge trapping at defect states and poorly confined 3D bulk phases.

These structural and optical analyses confirm that the hetero-scaffold enables spatially and dimensionally homogeneous X-type quasi-2D perovskites, establishing a spatially uniform carrier-confinement landscape for efficient and spectrally narrow light emission.

https://doi.org/10.1038/s41565-026-02208-y

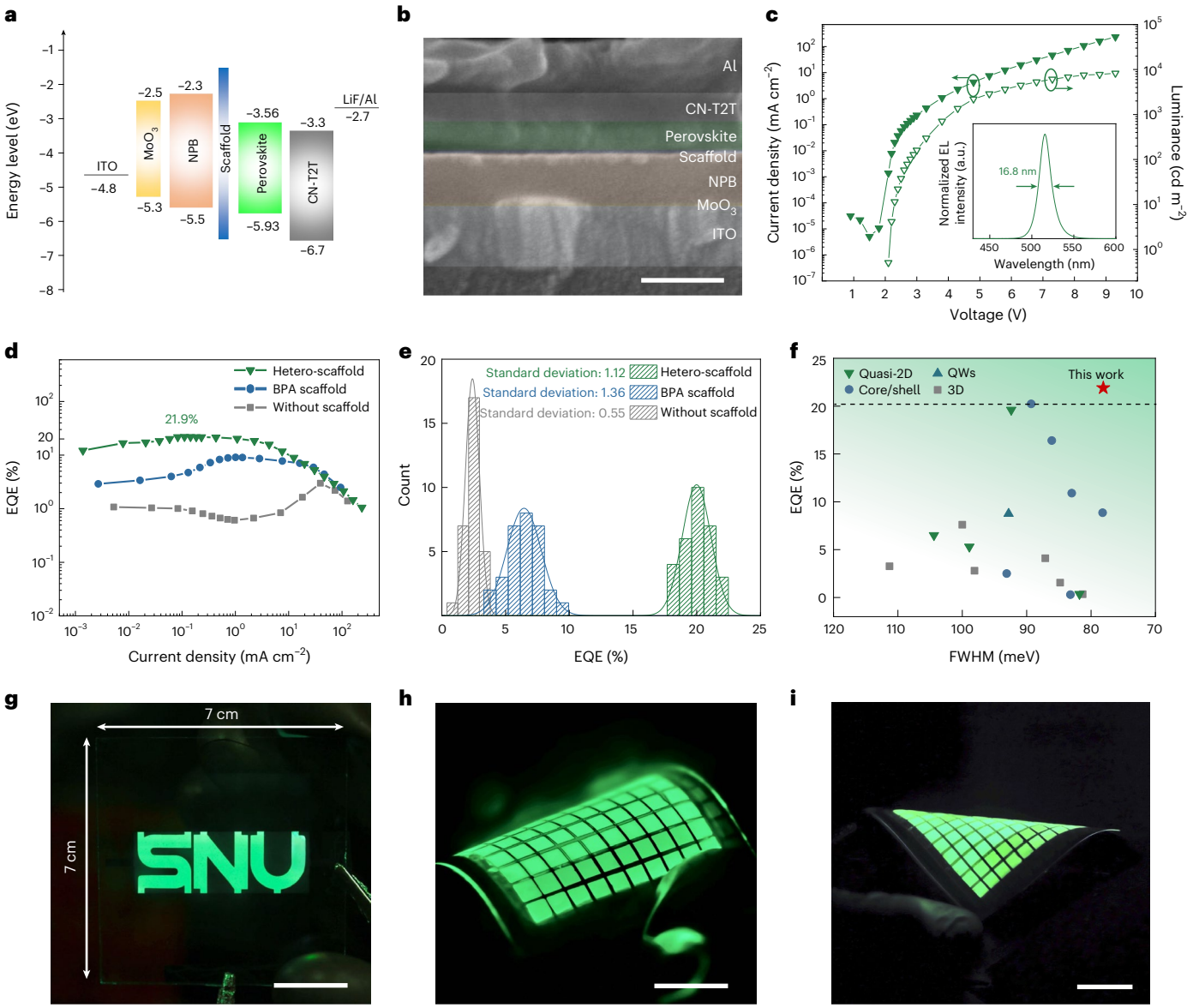

Fig. 4 | PeLED performance and large-area devices. a, Energy-level diagram of the PeLED device stack. ITO, indium tin oxide; MoO_3, molybdenum trioxide; NPB, *N*,*N*′-bis(naphthalen-1-yl)-*N*,*N*′-bis(phenyl)-benzidine; CN-T2T, 3′,3‴,3⁗′′-(1,3,5-triazine-2,4,6-triyl) tris(([1,1′-biphenyl]-3-carbonitrile)). **b**, Cross-sectional view of the PeLED device stack. Scale bar, 100 nm. **c**, *J*–*V*–*L* (filled triangles indicate the current density; hollow triangles indicate the luminance) characteristics of quasi-2D PeLEDs based on the hetero-scaffold. Inset: EL spectra of PeLEDs based on the hetero-scaffold. **d**, EQE versus current density curves for the PeLEDs based on different scaffolds. **e**, EQE histogram of PeLEDs based on different scaffolds. **f**, Summary of the reported vapour-deposited PeLED characteristics in terms of maximum EQE and EL linewidth. **g**–**i**, Photographs of large-area PeLED devices (operated at 3 V), showing Seoul National University (SNU) logo (**g**) and flexible 10 × 10 passive matrix (**h**,**i**) (active area = 4.5 mm × 4.5 mm). Scale bars, 2 cm.

LED performance

Building on the scaffold-assisted spatial and dimensional homogeneity of quasi-2D perovskite films, we fabricated PeLEDs using *N*,*N*′-bis(naphthalen-1-yl)-*N*,*N*′-bis(phenyl)-benzidine (NPB) and [1,1′-biphenyl]-3-carbonitrile, 3′,3‴,3⁗′′-(1,3,5-triazine-2,4,6-triyl)tris-(CN-T2T) as hole and electron transport layers, respectively (Fig. 4a,b, Supplementary Fig. 31 and Supplementary Table 5). The resulting PeLEDs exhibited a low turn-on voltage below 2.2 V, attributed to efficient hole and electron injections (Fig. 4c and Supplementary Fig. 32).

PeLEDs fabricated without a scaffold and with the BPA scaffold exhibited low maximum EQEs of 3.0% and 9.1%, respectively. PeLEDs based on the LiF-only scaffold also showed low maximum EQE of <10%, failing to achieve the quasi-2D phases but instead forming the bulky 3D phases without carrier confinement (Supplementary Fig. 33). By contrast, the hetero-scaffold PeLEDs showed a maximum EQE of 21.9%, based on angular EL measurements[40], which is the highest reported efficiency so far for vapour-deposited PeLEDs (Fig. 4d, Supplementary Figs. 34 and 35, and Supplementary Table 6). The EQE histogram of the hetero-scaffold PeLEDs (average = 20.0 ± 1.1%, 30 devices) further demonstrates that our all-vapour-deposited structure enables highly reproducible PeLEDs with efficient green EL (Fig. 4e). Here, careful control of the LiF thickness (~2 nm) within the hetero-scaffold is shown to be essential for enabling quasi-2D phase formation while avoiding unnecessary resistive losses, thereby ensuring balanced carrier injection and allowing the simultaneous realization of high luminance (>8,000 cd m^{-2}) and high EQE in vapour-deposited PeLEDs (Supplementary Fig. 36).

Moreover, the PeLEDs exhibited high spectral purity, with an extremely narrow FWHM of 78.5 meV (16.8 nm), surpassing previously reported vapour-deposited PeLEDs (Fig. 4f, Extended Data Fig. 9 and

Supplementary Table 7). In addition, PeLEDs with the hetero-scaffold exhibited greatly improved operational stability, achieving a half-lifetime (T_{50}) of >1,500 min under continuous operation at 100 cd m^{-2}, which is over 50 times longer than that of devices without a scaffold (<15 min) or with BPA scaffold (<30 min) (Supplementary Fig. 37). These results highlight the benefit of our strategy, where spatial and dimensional homogeneity leads to excellent optical characteristics. The scalability and versatility of our approach were further demonstrated with large-area devices and flexible LED arrays (Fig. 4g–i), which showed uniform emission from the turn-on voltage up to a high driving voltage (7 V) (Extended Data Fig. 10). These results suggest strong potential for broad applications not only in next-generation display technologies but also in the lighting and signage industries.

Conclusion

We synthesized X-type quasi-2D perovskites in vacuum by co-evaporating perovskite precursors with a halide-site-substituting organic spacer, BPA, through a thermodynamically guided crystallization pathway that enables high phase purity of quasi-2D nanostructures. The BPA spacer enabled the formation of a stable intermediate and quasi-2D structure during crystallization, thereby achieving thermodynamic phase pinning that cannot be achieved with conventional A-type quasi-2D structures, which undergo thermodynamic phase de-trapping. Furthermore, BPA simultaneously forms a self-assembled hetero-scaffold with LiF, establishing structural coherence at the interface between the quasi-2D perovskite lattice and the underlying layer, which has been a critical challenge in vapour-deposited perovskites. This enabled uniform and controlled crystallization of quasi-2D phases while suppressing low-*n*, 0D and bulk 3D phases. Nanoscale correlations among optical, chemical and morphological properties confirmed that this structural control produces narrow-distributed medium-*n* quasi-2D perovskite films with spatially and dimensionally homogeneous phase distributions, strong exciton confinement and high PLQY of >85%. As a result, PeLEDs exhibit ultra-narrow emission with an FWHM of 78.5 meV and an EQE of 21.9%, the highest efficiency reported for vapour-deposited PeLEDs, together with excellent scalability across large-area, flexible and patterned platforms. These findings establish a robust vapour-phase strategy for efficient perovskite emitters with controlled phase homogeneity and spectral purity, while its extension to conjugated organic spacer/scaffold chemistries remains an important route towards improved charge transport, efficiency and device stability.

Online content

Any methods, additional references, Nature Portfolio reporting summaries, source data, extended data, supplementary information, acknowledgements, peer review information; details of author contributions and competing interests; and statements of data and code availability are available at https://doi.org/10.1038/s41565-026-02208-y.

References

1. Tan, Z.-K. et al. Bright light-emitting diodes based on organometal halide perovskite. *Nat. Nanotechnol.* **9**, 687–692 (2014).
2. Kim, Y.-H. et al. Multicolored organic/inorganic hybrid perovskite light-emitting diodes. *Adv. Mater.* **27**, 1248–1254 (2015).
3. Cho, H. et al. Overcoming the electroluminescence efficiency limitations of perovskite light-emitting diodes. *Science* **350**, 1222–1225 (2015).
4. Fakharuddin, A. et al. Perovskite light-emitting diodes. *Nat. Electron.* **5**, 203–216 (2022).
5. Kim, J. S. et al. Ultra-bright, efficient and stable perovskite light-emitting diodes. *Nature* **611**, 688–694 (2022).
6. Han, T.-H. et al. A roadmap for the commercialization of perovskite light emitters. *Nat. Rev. Mater.* **7**, 757–777 (2022).
7. Kong, L. et al. Fabrication of red-emitting perovskite LEDs by stabilizing their octahedral structure. *Nature* **631**, 73–79 (2024).
8. Shin, M. et al. Modulation of growth kinetics of vacuum-deposited $CsPbBr_3$ films for efficient light-emitting diodes. *ACS Appl. Mater. Interfaces* **12**, 1944–1952 (2020).
9. Abzieher, T. et al. From groundwork to efficient solar cells: on the importance of the substrate material in co-evaporated perovskite solar cells. *Adv. Funct. Mater.* **31**, 2104482 (2021).
10. Luo, J. et al. Vapour-deposited perovskite light-emitting diodes. *Nat. Rev. Mater.* **9**, 282–294 (2024).
11. Li, J. et al. Efficient all-thermally evaporated perovskite light-emitting diodes for active-matrix displays. *Nat. Photon.* **17**, 435–441 (2023).
12. Svane, K. L. et al. How strong is the hydrogen bond in hybrid perovskites? *J. Phys. Chem. Lett.* **8**, 6154–6159 (2017).
13. Maufort, A. et al. Elucidating the non-covalent interactions that trigger interdigitation in lead-halide layered hybrid perovskites. *Inorg. Chem.* **63**, 5568–5579 (2024).
14. Wang, L. et al. Effect of post-annealing on thermally evaporated reduced-dimensional perovskite LEDs. *Appl. Phys. Lett.* **120**, 081107 (2022).
15. Du, P. et al. Efficient and large-area all vacuum-deposited perovskite light-emitting diodes via spatial confinement. *Nat. Commun.* **12**, 4751 (2021).
16. Dong, Z. et al. Intermediate phase evolution for stable and oriented evaporated wide-bandgap perovskite solar cells. *Nat. Mater.* **25**, 635–642 (2026).
17. Bu, T. et al. Modulating crystal growth of formamidinium–caesium perovskites for over 200 cm^2 photovoltaic sub-modules. *Nat. Energy* **7**, 528–536 (2022).
18. Park, S. M., Abtahi, A., Boehm, A. M. & Graham, K. R. Surface ligands for methylammonium lead iodide films: surface coverage, energetics, and photovoltaic performance. *ACS Energy Lett.* **5**, 799–806 (2020).
19. Dunlap, J. H. et al. Continuous flow synthesis of pyridinium salts accelerated by multi-objective Bayesian optimization with active learning. *Chem. Sci.* **14**, 8061–8069 (2023).
20. Xiong, S. et al. Reducing nonradiative recombination for highly efficient inverted perovskite solar cells via a synergistic bimolecular interface. *Nat. Commun.* **15**, 5607 (2024).
21. Brown, A. A. M. et al. Self-assembly of a robust hydrogen-bonded octylphosphonate network on cesium lead bromide perovskite nanocrystals for light-emitting diodes. *Nanoscale* **11**, 12370–12380 (2019).
22. Fu, G. et al. Effect of intramolecular geometry in phosphonic acid on surface passivation and lead immobilization in perovskite solar cells. *ACS Energy Lett.* **10**, 5457–5465 (2025).
23. Xiao, Z. et al. Efficient perovskite light-emitting diodes featuring nanometre-sized crystallites. *Nat. Photon.* **11**, 108–115 (2017).
24. Wang, K. et al. Suppressing phase disproportionation in quasi-2D perovskite light-emitting diodes. *Nat. Commun.* **14**, 397 (2023).
25. Kim, N. et al. Highly efficient vacuum-evaporated $CsPbBr_3$ perovskite light-emitting diodes with an electrical conductivity enhanced polymer-assisted passivation layer. *ACS Appl. Mater. Interfaces* **13**, 37323–37330 (2021).
26. Vaynzof, Y. The future of perovskite photovoltaics—thermal evaporation or solution processing? *Adv. Energy Mater.* **10**, 2003073 (2020).
27. Wang, Z. et al. Thermally evaporated metal halide perovskites and their analogues: film fabrication, applications and beyond. *Small Methods* **9**, 2301633 (2025).
28. Kim, B.-S., Gil-Escrig, L., Sessolo, M. & Bolink, H. J. Deposition kinetics and compositional control of vacuum-processed $CH_3NH_3PbI_3$ perovskite. *J. Phys. Chem. Lett.* **11**, 6852–6859 (2020).

29. Wood, C., Li, H., Winget, P. & Brédas, J.-L. Binding modes of fluorinated benzylphosphonic acids on the polar ZnO surface and impact on work function. *J. Phys. Chem. C* **116**, 19125–19133 (2012).
30. Wagstaffe, M. et al. An experimental investigation of the adsorption of a phosphonic acid on the anatase TiO_2(101) surface. *J. Phys. Chem. C* **120**, 1693–1700 (2016).
31. Yang, L. et al. Modulating binding strength and acidity of benzene-derivative ligands enables efficient and hysteresis-free perovskite/silicon tandem solar cells. *Angew. Chem. Int. Ed.* **64**, e202500350 (2025).
32. Park, S. et al. Replacing conventional battery electrolyte additives with dioxolone derivatives for high-energy-density lithium-ion batteries. *Nat. Commun.* **12**, 838 (2021).
33. Liang, J. et al. A gradient oxy-thiophosphate-coated Ni-rich layered oxide cathode for stable all-solid-state Li-ion batteries. *Nat. Commun.* **14**, 146 (2023).
34. Zhao, B. et al. Efficient light-emitting diodes from mixed-dimensional perovskites on a fluoride interface. *Nat. Electron.* **3**, 704–710 (2020).
35. Warby, J. H. et al. Revealing factors influencing the operational stability of perovskite light-emitting diodes. *ACS Nano* **14**, 8855–8865 (2020).
36. Jang, K. Y., Chang, S. E., Kim, D., Yoon, E. & Lee, T. Nanocrystalline perovskites for bright and efficient light-emitting diodes. *Adv. Mater.* **37**, 2415648 (2025).
37. Frohna, K. et al. The impact of interfacial quality and nanoscale performance disorder on the stability of alloyed perovskite solar cells. *Nat. Energy* **10**, 66–76 (2024).
38. Xing, G. et al. Transcending the slow bimolecular recombination in lead-halide perovskites for electroluminescence. *Nat. Commun.* **8**, 14558 (2017).
39. Jiang, Y. et al. Reducing the impact of Auger recombination in quasi-2D perovskite light-emitting diodes. *Nat. Commun.* **12**, 336 (2021).
40. Jeong, S.-H. et al. Characterizing the efficiency of perovskite solar cells and light-emitting diodes. *Joule* **4**, 1206–1235 (2020).

[1]Department of Materials Science and Engineering, Seoul National University, Seoul, Republic of Korea. [2]Department of Chemical Engineering and Biotechnology, University of Cambridge, Cambridge, UK. [3]Department of Physics, Cavendish Laboratory, University of Cambridge, Cambridge, UK. [4]Institute of Engineering Research, Soft Foundry, Research Institute of Advanced Materials, Seoul National University, Seoul, Republic of Korea. [5]Interdisciplinary Program in Bioengineering, Seoul National University, Seoul, Republic of Korea. [6]SN Display Co., Ltd., Seoul, Republic of Korea. [7]These authors contributed equally: Chan-Yul Park, Joo Sung Kim, Xian Wei Chua. ✉e-mail: sds65@cam.ac.uk; twlees@snu.ac.kr

Methods

Materials

Caesium bromide (CsBr) and molybdenum oxide (MoO_3) were purchased from Sigma-Aldrich. Lead bromide ($PbBr_2$ > 98.0% (T)) was purchased from TCI. Benzylphosphonic acid (BPA; >97%) was purchased from Acros Organics. *N*,*N*′-Bis(naphthalen-1-yl)-*N*,*N*′-bis(phenyl)-benzidine (NPB) was purchased from OSM. [1,1′-Biphenyl]-3-carbonitrile, 3′,3‴,3⁗-(1,3,5-triazine-2,4,6-triyl) tris- (CN-T2T) was purchased from Chanchun Tuocai Chem. LiF was supplied by FOOSUNG. Unless otherwise stated, all materials were used without purification.

$(CsPbBr_3)_{n-1}Cs_2PbBr_2BPA_2$ quasi-2D perovskite films preparation

A thermal evaporator with a high vacuum (<10^{-5} Pa) is essential to ensure a long mean free path for appropriate evaporation without any disruption by impurities. LiF and BPA scaffold layer were deposited with thermal evaporation (Bodeum thermal evaporator). CsBr, $PbBr_2$ and BPA are co-evaporated from separate sources, each precisely controlled by a separate power supply. For the exact thickness control of each source, CsBr, $PbBr_2$ and BPA sources were calibrated by controlling tooling factors. Because scaffold layer and co-evaporated BPA molecule delay the crystallization of perovskite, we adopted a substrate heating strategy with heater in the vacuum chamber. We controlled the deposition rates of CsBr, $PbBr_2$ and BPA gold quartz crystal sensors for precise monitoring. While we maintained the substrate temperature as 80 °C, rates of each source (CsBr, $PbBr_2$ and BPA) using thermal evaporation were fixed at 1.66 Å s^{-1}, 1.43 Å s^{-1} and 1.1 Å s^{-1}, respectively.

DFT calculations

Crystal structure optimization for PEA_2PbBr_4 and $Cs_2PbBr_2(BPA)_2$ were performed using the Vienna Ab initio Simulation Package (VASP)[41,42] with a projector augmented-wave method[43,44] where valence states of H, C, N, O, Pb and Br were treated explicitly by $1(1s^1)$, $4(2s^22p^2)$, $5(2s^22p^3)$, $6(2s^22p^4)$, $14(5d^{10}6s^26p^2)$ and $7(4s^24p^5)$ electrons, respectively. The Perdew–Burke–Ernzerhof exchange-correlation functional (PBE)[45] with the Grimme D3[46] scheme for van der Waals (vdW) corrections was used with a plane-wave kinetic energy cut-off of 700 eV and a 4 × 4 × 1 *Γ*-centred *k*-mesh. The convergence criteria were set to 10^{-8} eV for total energy and 10^{-2} eV $Å^{-1}$ for atomic forces.

Perovskite film characterization

Surface roughness and surface potential were characterized by AFM (NX-10). Surface morphology (SEM images) and elemental composition (EDS analysis) were examined using a field-emission scanning electron microscope (SIGMA). XPS and ultraviolet photoelectron spectroscopy (UPS) were performed with a photoelectron spectrometer (Versaprobe III, Ulvac-phi). A monochromatic Al Kα source (1,486.6 eV) was used for XPS, while He I radiation (21.2 eV) was used for UPS. Steady-state photoluminescence (PL) spectra and PLQY were measured with a JASCO FP-8500 spectrofluorometer, and UV–Vis absorption spectra were obtained using a JASCO V-770 spectrophotometer. Transient PL decay dynamics were measured with a FluoTime 300 spectrometer, using a picosecond-pulse laser diode head (LDH-P-C-405B, PicoQuant, 405 nm excitation). The emission decay was collected by a photon-counting detector (PMA Hybrid 07) and analysed using a time-correlated single-photon-counting module (PicoHarp, PicoQuant) to extract PL lifetimes. For temperature-dependent PL measurements, samples were mounted in a cryostat (Advanced Research Systems) under vacuum, and the emission spectra are subsequently obtained by using a 405 nm laser diode (PicoQuant).

Scanning transmission electron microscopy measurement

Scanning transmission electron microscopy (STEM) images of quasi-2D perovskites were acquired using a JEM-ARM200F (NEOARM) microscope operating at an acceleration voltage of 200 kV. To minimize air exposure and electron beam-induced damage, STEM specimens were prepared entirely in a glove box. We prepared samples on carbon grids by vapour deposition. The prepared grids were transferred directly within the chamber by maintaining the N_2 atmosphere using a transfer vessel.

Grazing-incidence X-ray diffraction measurements

GIWAXS measurements were carried out at beamline 3C of the Pohang Accelerator Laboratory (PAL), Republic of Korea. The incident X-ray beam (λ = 1.0973 Å) was fixed at an angle of 0.2° relative to the sample surface, and Eiger4M was used to detect the scattered X-ray beam. PLS-II 3C SAXS beamline data plot programme, MATLAB (0.1 ver.) and Zenodo were used to analyse the data[47].

Transient absorption spectroscopy measurement

Transient absorption spectroscopy measurements were performed on a HARPIA-TA system (Light Conversion). The output of a Yb:KGW laser (PHAROS, 1,035 nm, 10 kHz repetition rate, 163 fs pulse width, Light Conversion) was divided into two paths. One beam was directed to an optical parametric amplifier (ORPHEUS-NEO) to generate the 355 nm pump pulse. The second beam was frequency-doubled using a BBO crystal and subsequently focused onto a 5 mm sapphire crystal to generate a low-intensity continuum probe in the UV range. The magic angle of 54.7° was set between the polarization of the pump and probe beams. A mechanical delay stage varied the time delays between the pump and the probe beams. The pump and probe beams were spatially overlapped on the sample, and the transmitted probe was collected using an Andor Kymera 193i spectrograph.

PLQY measurements

PLQY measurements were performed using an integrating sphere set-up[48]. Samples were excited with a 405 nm laser at various excitation powers. The emitted and excitation signals were collected through an optical fibre connected to a Teledyne SpectraPro HRS-500 spectrograph, and spectra were recorded using a silicon CCD (Teledyne PIXIS 1024).

Hyperspectral PL microscopy

Spectrally resolved PL maps were acquired using an IMA hyperspectral microscope (Photon Etc.) under wide-field continuous-wave laser excitation at 405 nm (ref. 49). The detection wavelength was spectrally scanned from 415 nm to 600 nm using a volume Bragg grating, with monochromatic images acquired successively at ~2 nm spectral resolution. At each detection wavelength, the system performed an automatic refocusing of the sample stage. The volume Bragg grating dispersed the light onto a 1,392 × 1,040 pixel silicon CCD detector, which was maintained at 0 °C by a thermoelectric cooler.

Confocal time-resolved PL microscopy

Confocal time-resolved PL microscopy was performed using a PicoQuant MicroTime 200 set-up. We used a 404 nm pulsed laser excitation (LDH-D-C-405, PicoQuant) at a repetition rate of 1 MHz. We used a ×100 air objective (Olympus MPlanFL N; numerical aperture, 0.9) for a focused, near-diffraction-limited excitation beam. The emission signal was separated from excitation light using a dichroic mirror (zt405rdc, Chroma). For time-resolved PL maps, both excitation and emission paths were raster scanned using a galvo mirror scanning system (FLIMbee). The PL was focused on a PMA Hybrid-42 detector (PicoQuant) for single-photon counting (time resolution, 25 ps) through a 75 µm pinhole, with a 425 nm long-pass filter in the detection path. The scan area is 20 µm × 20 µm, with a pixel size of 78 nm in both *x* and *y* directions.

Contact angle measurements

Contact angles were measured with deionized water and diiodomethane at room temperature and 60% relative humidity by using a Smart Drop system (Femtofab).

Ellipsometry measurements

A variable-angle spectroscopic ellipsometer (VASE, J.A. Woollam) was used to measure the refractive index and extinction coefficient of the perovskite layer for optical simulation. Ellipsometry data were collected over a wavelength range of 200–1,650 nm, with detection angles from 45° to 75° in 5° increments.

Fabrication of PeLEDs

Patterned indium tin oxide (ITO) (70 nm, 25 mm × 25 mm) glass substrates were sequentially sonicated in deionized water, acetone and 2-propanol for 15 min each, followed by boiling in 2-propanol for 30 min. The surface of ITO substrates was treated with O_2 plasma with RIE equipment to achieve reactive surface for MoO_3. We deposited MoO_3 for HIL and NPB for HTL in high vacuum state (<10^{-7} torr), and then the LiF scaffold was deposited in the same chamber with thermal evaporation. After HIL, HTL and LiF scaffold evaporation, the substrates were transferred to the perovskite evaporation chamber. The sample was loaded into the chamber until the vacuum state reached 10^{-5} torr, and the BPA scaffold layer was deposited with a fixed evaporation rate of 0.1 Å s^{-1} by a thermal evaporation method. Sequentially, perovskite using CsBr, $PbBr_2$ and BPA precursor is formed during evaporation with 80 °C of substrate heating temperature. Samples were transferred to the previous organic/metal chamber (< 10^{-7} torr) to sequentially deposit CN-T2T (35 nm), LiF (1.2 nm) and Al (100 nm). The active area of 4.3 mm^2 was defined with the shadow mask during deposition of the cathode. Finally, in a glove box under a tightly controlled N_2 atmosphere (O_2 < 1.0 ppm, H_2O < 0.5 ppm), the fabricated vapour-deposited PeLEDs were encapsulated with a glass lid and UV-curable epoxy resin, followed by 15 min of UV irradiation (365 nm).

Characterization of PeLEDs

The EL efficiency of the fabricated PeLEDs was characterized using a Keithley 236 source-measurement unit and a Minolta CS-2000 spectroradiometer. The full angular EL distribution was measured by rotating the device relative to the fixed spectroradiometer, and then the exact EQE was calculated based on the Lambertian angle factor. By using an electrochemical impedance spectroscopy workstation (SP-200 potentiostat, Biologic), capacitance–voltage measurement was conducted to evaluate charge balance in the LED devices.

Optical simulation of PeLEDs

Optical simulations of angle-dependent EL intensity were performed using Python code manually implemented by the author based on the classical dipole model, the transfer matrix method and additional custom algorithms. The simulation results were validated by comparison with those from commercial optical simulation software. The input parameters included the PL spectra, emission zone distribution, horizontal dipole orientation ratio in the emitting layer, as well as the refractive indices and thicknesses of each layer. The refractive indices were measured using variable-angle spectroscopic ellipsometry.

Data availability

All the data supporting this paper are available in the form of Source Data files and the supplementary material. Source data are provided with this paper.

References

41. Kresse, G. & Furthmüller, J. Efficient iterative schemes for *ab initio* total-energy calculations using a plane-wave basis set. *Phys. Rev. B* **54**, 11169–11186 (1996).
42. Kresse, G. & Furthmüller, J. Efficiency of ab-initio total energy calculations for metals and semiconductors using a plane-wave basis set. *Comput. Mater. Sci.* **6**, 15–50 (1996).
43. Kresse, G. & Joubert, D. From ultrasoft pseudopotentials to the projector augmented-wave method. *Phys. Rev. B* **59**, 1758–1775 (1999).
44. Blöchl, P. E. Projector augmented-wave method. *Phys. Rev. B* **50**, 17953–17979 (1994).
45. Perdew, J. P., Burke, K. & Ernzerhof, M. Generalized gradient approximation made simple. *Phys. Rev. Lett.* **78**, 1396 (1997).
46. Grimme, S., Antony, J., Ehrlich, S. & Krieg, H. A consistent and accurate *ab initio* parametrization of density functional dispersion correction (DFT-D) for the 94 elements H-Pu. *J. Chem. Phys.* **132**, 154104. (2010).
47. Kim, Y. Y., Kim, J. & Kim, N. pGIXS: PLS-II 3C SAXS beamline data plot program with MATLAB. *Zenodo* https://doi.org/10.5281/zenodo.7042272 (2022).
48. De Mello, J. C., Wittmann, H. F. & Friend, R. H. An improved experimental determination of external photoluminescence quantum efficiency. *Adv. Mater.* **9**, 230–232 (1997).
49. Wei, Z., Dubajic, M., Chosy, C., Kahmann, S. & Stranks, S. D. Photoluminescence microscopy of optoelectronic materials. *Nat. Rev. Methods Prim.* **5**, 37 (2025).

Author contributions

C.-Y.P., J.S.K. and X.W.C. equally contributed to this work. C.-Y.P., J.S.K. and T.-W.L. initiated and designed the study. C.-Y.P. fabricated the PeLED devices. C.-Y.P. and M.-J.S. conducted the GIWAXS analysis. X.W.C., J.S.K. and S.D.S. designed and conducted the spectroscopic experiments, including hyperspectral photoluminescence microscopy and transient absorption spectroscopy, and analysed and interpreted the data. C.-Y.P., J.S. and K.-H.L. conducted the PL and UV–Vis spectroscopy measurements. Y.-K.J. calculated the lattice structure of quasi-2D perovskites using DFT simulation. E.Y. conducted the FTIR, EDS, XPS and UPS analyses. C.-Y.P. and J.S.K. analysed the solid-state ^{31}P-NMR to verify the structure of X-type quasi-2D perovskites. X.W.C. performed time-resolved confocal photoluminescence microscopy. E.Y., S.E.C., J.S. and B.-H.C. conducted the morphological analysis, including SEM and AFM measurements. S.E.C. conducted the ellipsometry measurements. C.-Y.P., H.-W.K. and S.K. conducted the design and fabrication of large-area PeLEDs. C.-Y.P. and E.Y. conducted the transient and temperature-dependent PL analysis. C.-Y.P. conducted the capacitance–voltage electrical analysis of devices. W.J.J. conducted the device optical simulation. J.P. analysed the Elliott fitting by deconvoluting peaks in UV–Vis spectroscopy. T.-W.L. and S.D.S. supervised the work. C.-Y.P. and J.S.K. drafted the first version of the paper with assistance from T.-W.L. All authors discussed the results and commented on the paper.

Funding

This work was supported by the National Research Foundation of Korea (NRF) grant funded by the Ministry of Science and ICT (MSIT) (RS202500560490 and 2022M3H4A1A04096380). S.D.S. acknowledges the European Research Council (ERC) under the European Union's Horizon 2020 research and innovation programme (HYPERION, grant agreement number 756962) and Horizon Europe (VAPOURISE, grant agreement number 101169608) research and innovation programmes. Views and opinions expressed are however those of the authors only and do not necessarily reflect those of the European Union or the European Research Council Executive Agency. Neither the European Union nor the granting authority can be held responsible for them. S.D.S. acknowledges the Royal Society and Tata Group (UF150033 and URF\R\221026). J.S.K. acknowledges European Union guarantee funding for Marie Skłodowska-Curie Actions Postdoctoral Fellowships 2024 (101200330). X.W.C. thanks the Agency for Science, Technology and Research (A*STAR, Singapore) for the National Science Scholarship. Y.-K.J. acknowledges UKRI guarantee funding for Marie Skłodowska-Curie

Actions Postdoctoral Fellowships 2021 (EP/X025756/1). Via our membership of the UK's HEC Materials Chemistry Consortium, which is funded by EPSRC (EP/X035859/1), this work used the ARCHER2 UK National Supercomputing Service (http://www.archer2.ac.uk). Y.-K.J. and S.D.S. acknowledge a Leverhulme Research Grant (RPG-2021-191).

Competing interests
The authors declare no competing interests.

Additional information
Extended data is available for this paper at https://doi.org/10.1038/s41565-026-02208-y.

Supplementary information The online version contains supplementary material available at https://doi.org/10.1038/s41565-026-02208-y.

Correspondence and requests for materials should be addressed to Samuel D. Stranks or Tae-Woo Lee.

Peer review information *Nature Nanotechnology* thanks Zhao-Kui Wang, Zhanhua Wei and the other, anonymous, reviewer(s) for their contribution to the peer review of this work.

https://doi.org/10.1038/s41565-026-02208-y

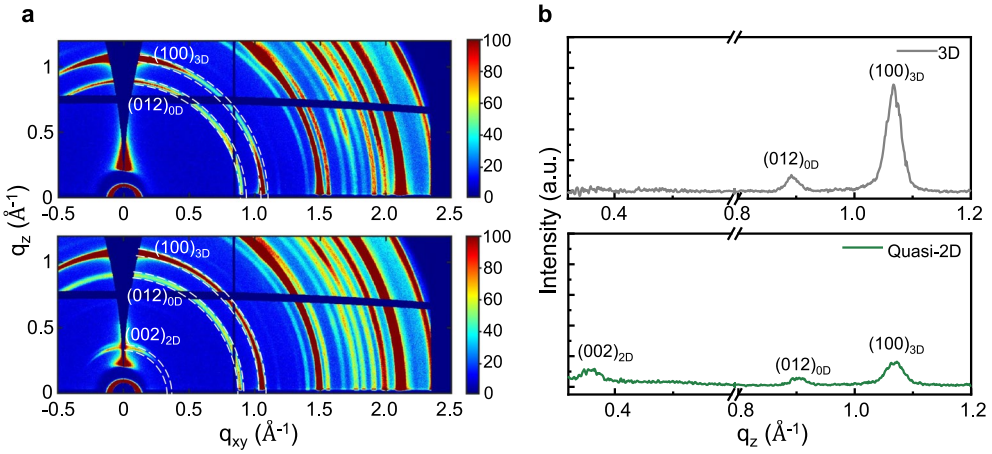

Extended Data Fig. 1 | GIWAXS profile of perovskite films. a, GIWAXS 2D patterns of 3D (upper panel) and X-type quasi-2D (bottom panel) perovskite film. **b**, GIWAXS 1D plot of 3D (upper panel) and X-type quasi-2D (bottom panel) perovskite film. For comparison, 3D perovskite film was fabricated by co-evaporating CsBr and $PbBr_2$ without the organic spacer. GIWAXS patterns of these films showed diffraction features corresponding to the emissive cubic 3D $CsPbBr_3$ phase at q = 1.07 $Å^{-1}$, d = 5.87 Å, together with the non-emissive 0D Cs_4PbBr_6 phase at q = 0.90 $Å^{-1}$, d = 6.98 Å. In contrast, the X-type quasi-2D perovskite film showed a strong out-of-plane diffraction peak at q = 0.35 $Å^{-1}$, d = 18.0 Å, assigned to the (002) plane of the 2D perovskite.

https://doi.org/10.1038/s41565-026-02208-y

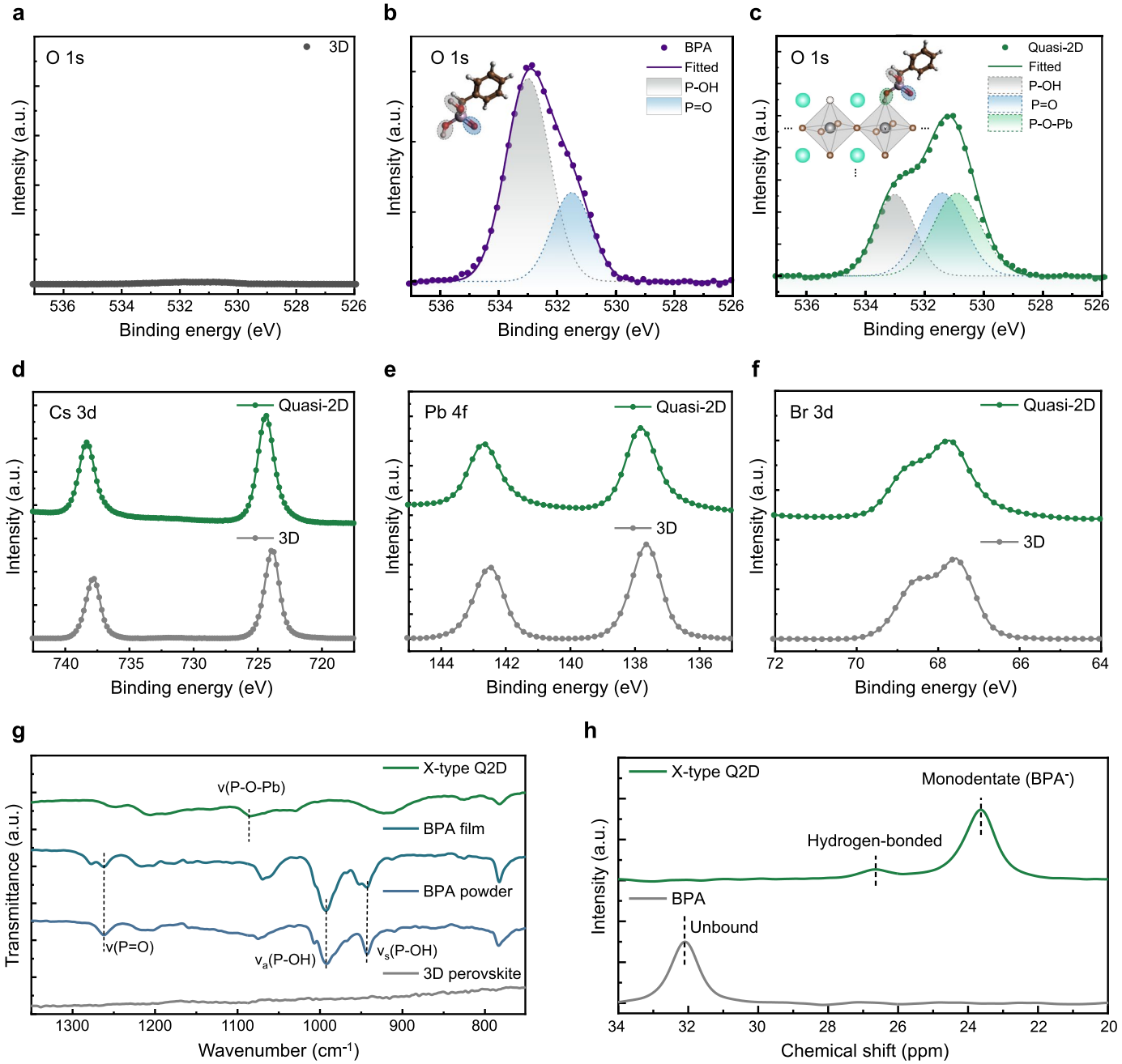

Extended Data Fig. 2 | Chemical analysis of vapour phase synthesized perovskite films. a-c, XPS O 1 s spectra of 3D $CsPbBr_3$ (**a**), BPA (**b**), and X-type quasi-2D (**c**) perovskite films. **d-e**, XPS Cs 3 d spectra (**d**), Pb 4 f spectra (**e**), and Br 3 d spectra (**f**) of 3D and quasi-2D perovskite films. **g**, FT-IR spectra of 3D perovskite (grey), BPA powder (navy), BPA film (blue), X-type quasi-2D perovskite (green). **h**, Solid-state ^{31}P-NMR of BPA powder (grey) and vapour-deposited X-type quasi-2D perovskite powder (green). While 3D perovskite without BPA showed no distinctive O 1 s feature, the X-type quasi-2D perovskite exhibited a new O 1 s signal associated with oxygen atoms from BPA. Pristine BPA molecules showed characteristic P–OH and P = O peaks at 533.0 and 531.5 eV, respectively, with a theoretical atomic ratio of 2:1. In contrast, the X-type quasi-2D perovskite exhibited an additional O 1 s peak at 531.0 eV, assigned to covalently bonded P–O–Pb species. The P–O–Pb and remaining P–OH components appeared in an approximately 1:1 atomic ratio, indicating that one P–OH groups in BPA undergoes deprotonation and coordinates to a Pb^{2+} centre in a monodentate configuration. FTIR and solid-state ^{31}P NMR analyses further confirmed the BPA binding mode. FTIR spectra showed the emergence of a new P–O–Pb vibration at 1070 cm^{-1}, along with a red-shifted and broadened P–OH vibration from 930 to 920 cm^{-1}. Solid-state ^{31}P NMR showed that the pristine BPA resonance at 32.09 ppm shifted upfield in the X-type quasi-2D perovskite. The spectrum contained a minor resonance assigned to hydrogen-bonded BPA at 26.04 ppm and a dominant resonance at 23.63 ppm corresponding to chemisorbed monodentate BPA^- species. These results provide detailed spectroscopic evidence that BPA forms monodentate P–O–Pb bonds within the X-type quasi-2D perovskite lattice.

https://doi.org/10.1038/s41565-026-02208-y

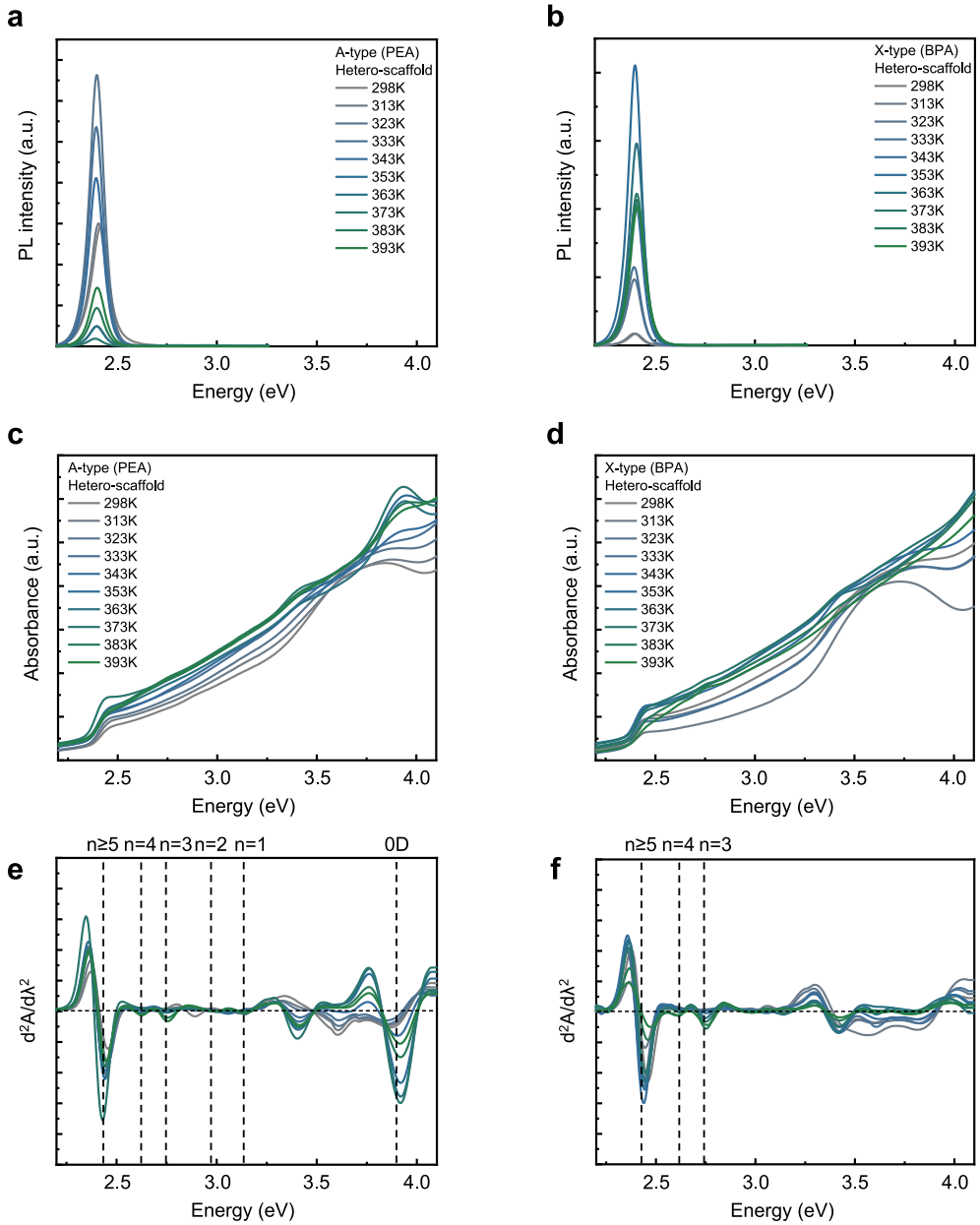

Extended Data Fig. 3 | Optical property of vapour-phase synthesized quasi-2D perovskites with different organic spacers on the hetero-scaffold. **a-b**, Steady-state PL spectra of A-type (**a**) and X-type (**b**) quasi-2D perovskite films at different back-heating temperatures. **c-d**, UV-Vis absorption spectra of A-type (**c**) and X-type (**d**) at different back-heating temperatures. **e-f**, Second derivative of UV-Vis absorption spectra of A-type (**e**) and X-type (**f**) quasi-2D perovskite films corresponding to **c** and **d**, each at different back-heating temperatures. To ensure that the comparison reflects intrinsic differences in phase formation rather than interfacial effects, all perovskite films were deposited on a bilayer scaffold consisting of the corresponding organic spacers onto thin lithium fluoride (LiF) layer on the substrate, which guides uniform crystallization across the film.

https://doi.org/10.1038/s41565-026-02208-y

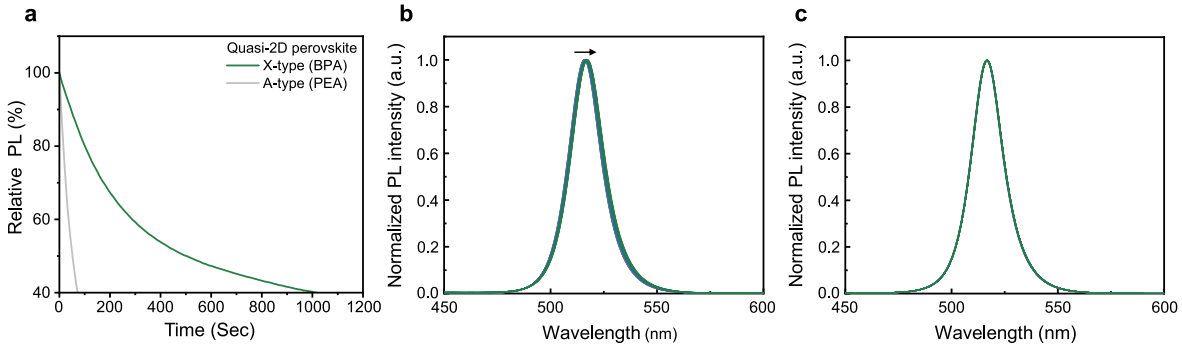

Extended Data Fig. 4 | Photostability of quasi-2D perovskite films with different organic spacers. a, Photostability of quasi-2D perovskite films with different organic spacers in ambient air with a relative humidity of 50 - 60%. **b**-**c**, Normalized PL spectra during the photostability measurement of A-type quasi-2D perovskites (**b**) and X-type quasi-2D perovskites (**c**). The red-shifted emission spectra of A-type quasi-2D after the photostability test can be ascribed to disproportionation toward higher-*n* or bulk 3D phases, whereas such disproportionation was suppressed in the X-type quasi-2D perovskites with improved photostability.

https://doi.org/10.1038/s41565-026-02208-y

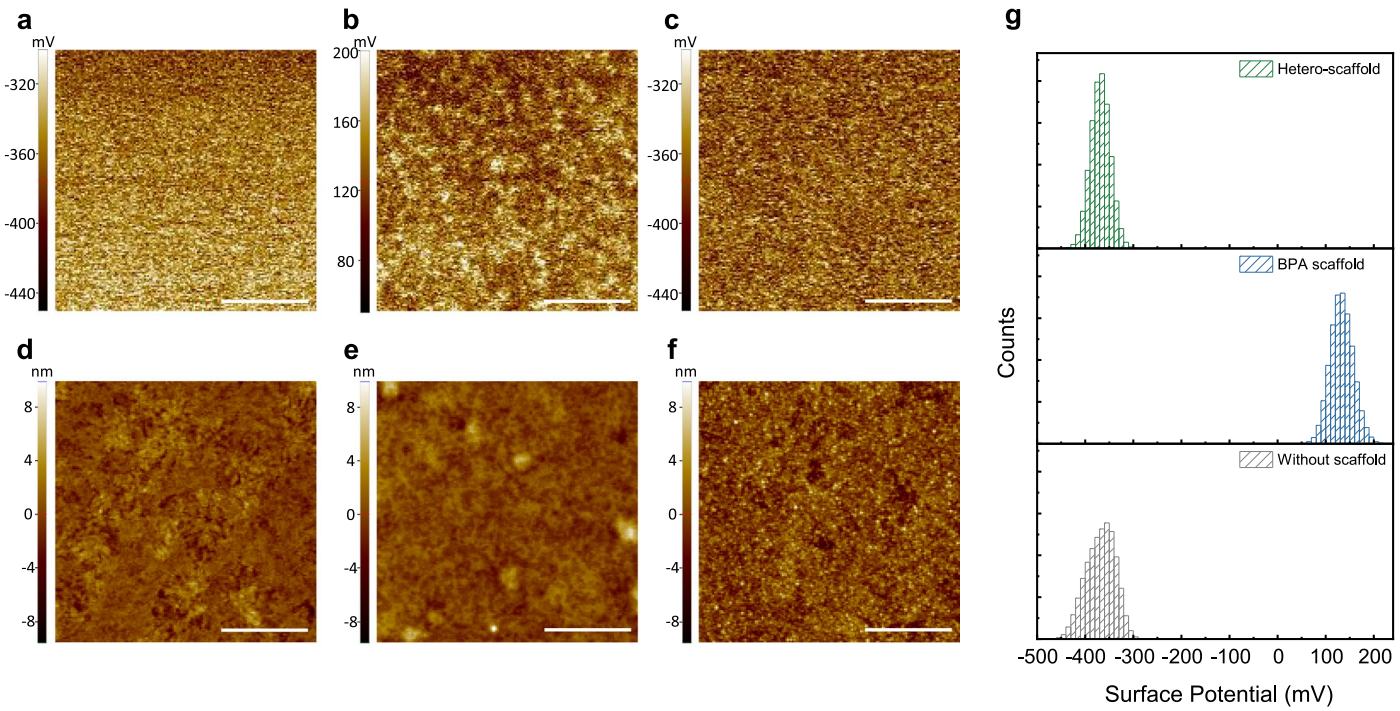

Extended Data Fig. 5 | Surface potential analysis of self-assembled scaffolds. **a-f**, KPFM mapping (**a-c**) and AFM topography images (**d-f**) of underneath NPB layer without a scaffold (**a, d**), with the BPA scaffold (**b, e**), and with the hetero-scaffold (**c, f**). Scale bar, 1 μm. **g**, Surface potential distribution of each scaffold. Compared with the NPB layer without a scaffold and BPA scaffold with locally aggregated non-uniform region, the hetero-scaffold provided overall uniform surface potential distribution.

https://doi.org/10.1038/s41565-026-02208-y

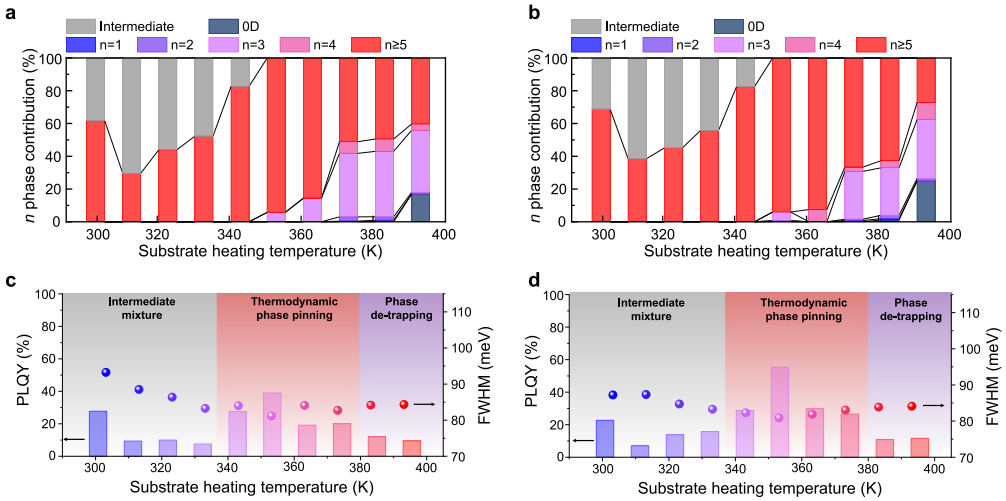

Extended Data Fig. 6 | Emissive properties of vapour-phase-synthesized quasi-2D perovskites with different scaffolds. a-b, *n*-phase contribution of vapour-phase-synthesized quasi-2D perovskite films without a scaffold (**a**) and with the BPA scaffold (**b**) at different back-heating temperatures. **c-d**, PLQY versus FWHM of quasi-2D perovskite films without a scaffold (**c**) and with the BPA scaffold (**d**) at different back-heating temperatures. Due to inhomogeneous surface-precursor interactions in crystallization process without a scaffold and with the BPA scaffold, trace amount of phase de-trapping was observed such as crystallization of low-*n* phases at ~353 K and Cs_4PbBr_6 0D phases at 393 K.

https://doi.org/10.1038/s41565-026-02208-y

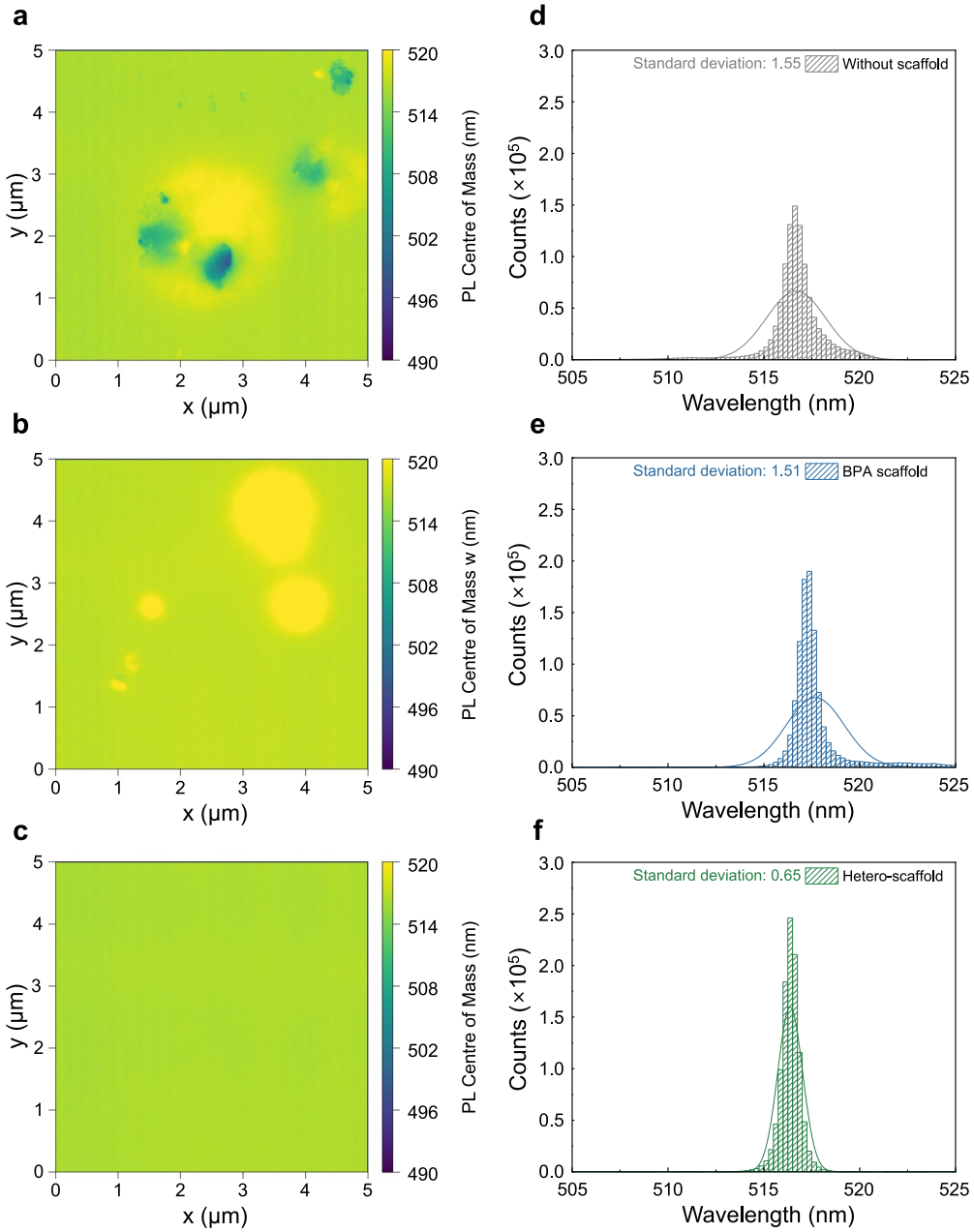

Extended Data Fig. 7 | Confocal photoluminescence maps of quasi-2D perovskite films with different scaffolds. Centre-of-mass (CoM) PL wavelength image (**a**-**c**) and corresponding histograms (**d**-**f**) of the quasi-2D perovskite films without a scaffold (**a**, **d**), with the BPA scaffold (**b**, **e**), and with the LiF/BPA hetero-scaffold (**c**, **f**). Scale bar, 5 μm. The CoM map reveals a distinct phase-segregated morphology, where blue-shifted emission from low-*n* quasi-2D phases appears in isolated regions surrounded by red-shifted emission associated with bulk 3D phases. This spectral inhomogeneity arises from stoichiometric imbalance induced by segregated BPA organic spacers during the early stage of crystallization, leading to lateral separation into BPA-rich (low-*n*) and BPA-poor (bulk-3D) domains. In contrast, the use of the hetero-scaffold template enables uniform alignment and distribution of BPA, resulting in stoichiometrically balanced crystallization across the substrate and achieving spatially uniform CoM maps without spectral deviation.

https://doi.org/10.1038/s41565-026-02208-y

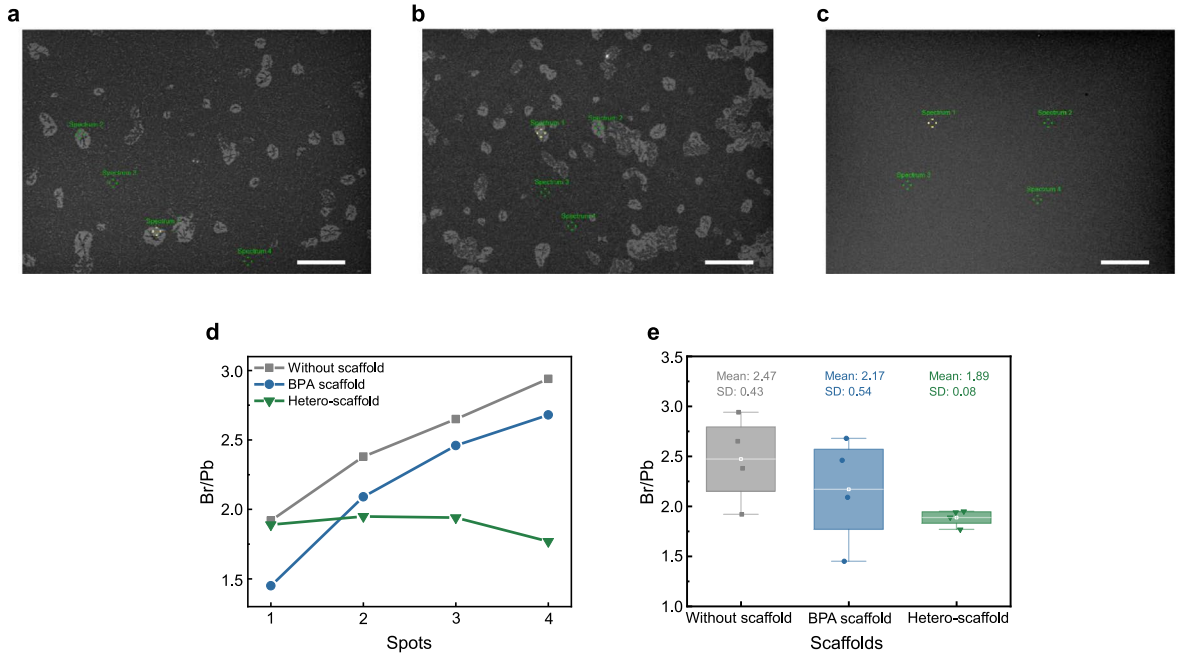

Extended Data Fig. 8 | Morphology of quasi-2D perovskite films with different scaffolds. a-c, SEM images of quasi-2D perovskite films grown without a scaffold (**a**), with BPA scaffold (**b**), and hetero-scaffold (**c**). Scale bar, 20 µm. **d-e**, Br/Pb ratio difference at each spot (**d**) and variation of Br/Pb ratio in each perovskite film (**e**). EDS point analysis was conducted to investigate stoichiometric deviations in phase-segregated regions. In the high-brightness areas near the segregated domains (spectra 1 and 2 in a and b), the Br/Pb ratio is substantially lower than that in surrounding regions (spectra 3 and 4). This suggests the formation of segregated low-*n* phases, in which a greater fraction of halide sites is occupied by BPA spacer molecules rather than Br atoms compared with bulk-like 3D phases. For each sample, the Br/Pb ratio distribution was obtained from four selected measurement points in a single EDS point-scan analysis. Data are presented as mean ± standard deviation (SD). The mean Br/Pb ratios of the perovskites grown without a scaffold and with the BPA scaffold were 2.47 ± 0.43 and 2.17 ± 0.54. In contrast, films grown on the hetero-scaffold show uniform morphology and a consistent Br/Pb ratio of 1.89 ± 0.08, with minimal deviation across the entire area.

https://doi.org/10.1038/s41565-026-02208-y

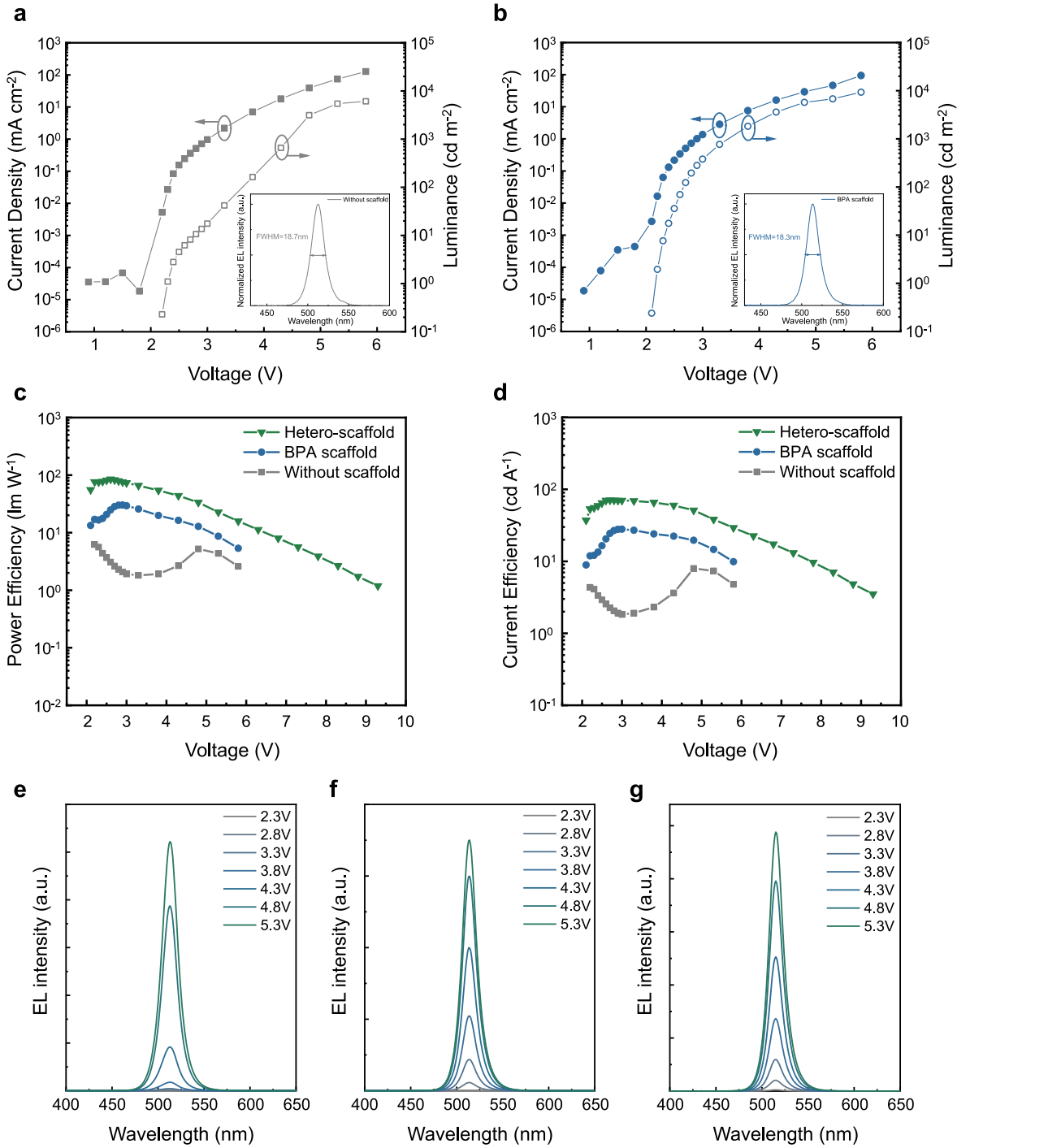

Extended Data Fig. 9 | Current-voltage-luminance characteristics of PeLEDs with different scaffolds. a-b, J–V–L characteristics of quasi-2D PeLEDs without a scaffold (**a**) and with the BPA scaffold (**b**). Insets: normalized EL spectra. **c**, Power efficiency versus voltage curves and **d**, current efficiency versus voltage curves of PeLEDs with different scaffolds. **e-g**, EL spectra at different driving voltages of PeLEDs without a scaffold (**e**), with the BPA scaffold (**f**), and with the hetero-scaffold (**g**).

https://doi.org/10.1038/s41565-026-02208-y

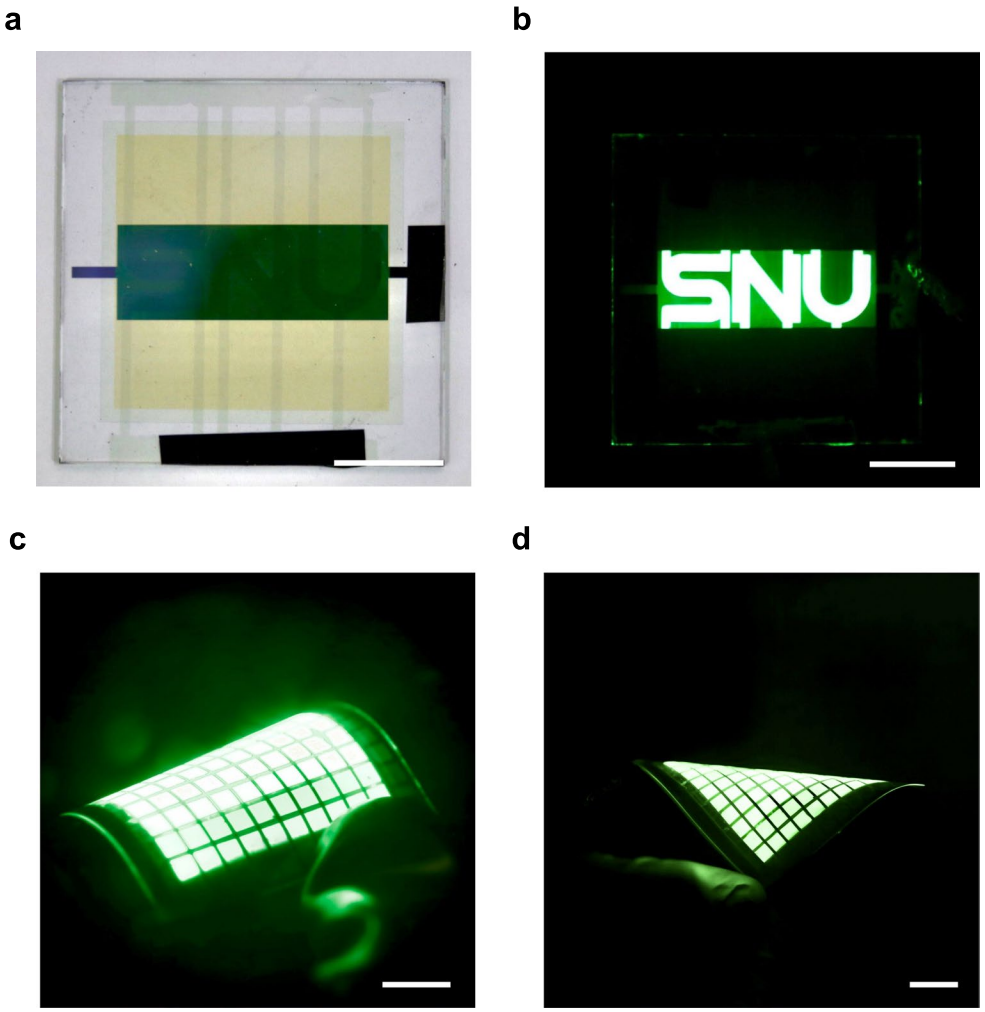

Extended Data Fig. 10 | Photographs of large-area devices. a-b, Photograph of a patterned large-area PeLED device before operation (**a**) and the corresponding device image during operation at 7 V (**b**). **c-d**, Photographs of a pixelated large-area flexible PeLED device under bending conditions, operated at 7 V, demonstrating mechanical robustness and uniform emission of all-vapour-deposited PeLEDs. Scale bar, 2 cm.